
Article:
Vidal, J, Cébron, D, Schaeffer, N et al. (1 more author) (2018) Magnetic fields driven by tidal mixing in radiative stars. Monthly Notices of the Royal Astronomical Society, 475 (4). pp. 4579-4594. ISSN 0035-8711

https://doi.org/10.1093/mnras/sty080

Monthly Notices
of the
ROYAL ASTRONOMICAL SOCIETY

MNRAS **475,** 4579–4594 (2018)
Advance Access publication 2018 January 10

doi:10.1093/mnras/sty080

Magnetic fields driven by tidal mixing in radiative stars

Jérémie Vidal,[1]★ David Cébron,[1] Nathanaël Schaeffer[1] and Rainer Hollerbach[2]

[1]*Université Grenoble Alpes, CNRS, ISTerre, F-38000 Grenoble, France*
[2]*Department of Applied Mathematics, University of Leeds, Leeds LS2 9JT, UK*

Accepted 2018 January 8. Received 2018 January 3; in original form 2017 November 16

ABSTRACT

Stellar magnetism plays an important role in stellar evolution theory. Approximatively 10 per cent of observed main sequence (MS) and pre-main-sequence (PMS) radiative stars exhibit surface magnetic fields above the detection limit, raising the question of their origin. These stars host outer radiative envelopes, which are stably stratified. Therefore, they are assumed to be motionless in standard models of stellar structure and evolution. We focus on rapidly rotating, radiative stars which may be prone to the tidal instability, due to an orbital companion. Using direct numerical simulations in a sphere, we study the interplay between a stable stratification and the tidal instability, and assess its dynamo capability. We show that the tidal instability is triggered regardless of the strength of the stratification (Brunt–Väisälä frequency). Furthermore, the tidal instability can lead to both mixing and self-induced magnetic fields in stably stratified layers (provided that the Brunt–Väisälä frequency does not exceed the stellar spin rate in the simulations too much). The application to stars suggests that the resulting magnetic fields could be observable at the stellar surfaces. Indeed, we expect magnetic field strengths up to several Gauss. Consequently, tidally driven dynamos should be considered as a (complementary) dynamo mechanism, possibly operating in radiative MS and PMS stars hosting orbital companions. In particular, tidally driven dynamos may explain the observed magnetism of tidally deformed and rapidly rotating Vega-like stars.

Key words: dynamo – hydrodynamics – instabilities – magnetic field – MHD – waves.

1 INTRODUCTION

1.1 Stellar magnetism

Stellar magnetic fields were first discovered in the Sun (Hale 1908) and in the chemically peculiar Ap star 78 Virginis (Babcock 1947). Stellar magnetism sparks growing interest, since it provides additional data to infer the dynamical processes occurring in stellar interiors. On one hand, it has been known for decades that magnetic fields are common in solar-like low-mass stars, in which magnetic fields have complex surface structures and time variabilities. Since the pioneering works of Larmor (1919), Parker (1955), Roberts (1968), Busse (1970), and many works in stellar magnetism have considered magnetic fields driven by thermochemical convection. Indeed, it is widely accepted that stellar magnetic fields originate from motions within the convective envelope, generating dynamo action (Parker 1979). Convectively driven dynamo action is supported by magnetohydrodynamic numerical simulations of both stellar and planetary fluid interiors (e.g. Glatzmaier & Roberts 1995; Brun et al. 2004; Schaeffer et al. 2017; Strugarek et al. 2017). Furthermore, reduced mean-field or flux-transport models can be tuned to reproduce magnetic cycles as observed for the Sun (e.g. Jouve & Brun 2007; Jouve et al. 2010; Charbonneau 2014) or solar-like stars (e.g. Jouve et al. 2010).

On the other hand, the magnetism of hot Ap/Bp stars, a group of intermediate-mass A/B stars showing strong chemical peculiarities, with outer radiative layers (i.e. stably stratified in density), is different from the magnetism of cool solar-like stars. Indeed, they display global dipolar fields, with typical amplitudes ranging from 300 G (Aurière et al. 2007) to thousands of Gauss, and seem remarkably stable over observational time (Donati & Landstreet 2009). Recently, magnetic fields with Gauss-level amplitudes have been detected in several stars (Blazère et al. 2016a,b), e.g. in Vega (Lignières et al. 2009; Petit et al. 2010) and in Sirius A (Petit et al. 2011). They form another class of magnetic stars defining the Vega-like stellar magnetism. Hence, there is a strong dichotomy, or magnetic desert, between strong and ultra-weak magnetic fields among hot stars (Lignières et al. 2013). More generally, astronomical observations show that between 5 per cent and 10 per cent of main-sequence (MS, e.g. Ap/Bp) and pre-main-sequence (PMS, e.g. Herbig Ae/Be) stars exhibit surface magnetic fields (Donati & Landstreet 2009; Braithwaite & Spruit 2017; Mathys 2017).

It is commonly accepted that stars form from a fully convective low-mass core, which grows through accretion during the protostellar phase (Palla & Stahler 1992; Behrend & Maeder 2001).

★ E-mail: jeremie.vidal@univ-grenoble-alpes.fr

However, hot stars undergo important changes in their interior structures before reaching the MS. Stellar models indicate that after the initial fully convective phase, a radiative core forms and grows in the whole star. This suggests that sun-like dynamo action does not occur in hot stars with thick outer radiative envelopes. However, in very massive stars, an innermost convective core may develop. Hence, the magnetic desert may result from the large variability of mechanisms generating magnetic fields in hot stars.

1.2 Proposed mechanisms in hot stars

The origin of stellar magnetism in hot stars remains elusive and debated (Neiner et al. 2014). The observed fields are often presumed to be fossil fields (Borra et al. 1982; Braithwaite & Spruit 2004), which were shaped during the stellar formation phase (Power et al. 2008) and might survive into later stages of stellar evolution. The observed strong dipolar fields of Ap/Bp stars are stable over time (Donati & Landstreet 2009), which is compatible with fossil fields. However, it seems difficult for rapidly rotating stars to reach stable magnetic equilibrium (Braithwaite & Cantiello 2012). Similarly, the fossil field model does not seem to predict the observed small scale and weak fields of Vega-like stars. It has been proposed that their magnetic field is at equilibrium but undergo a dynamical evolution before reaching an equilibrium state (Braithwaite & Cantiello 2012). Moreover, the fossil field origin has also been questioned for the magnetic field of PMS Herbig Ae/Be stars, which are expected to be the precursors of magnetic Ap/Bp stars on the PMS phase (Alecian et al. 2012). However, the recently observed dramatic change of the surface magnetic field of HD 190073 (Alecian et al. 2013), which possibly hosts a small inner convective core, could result from interactions with a dynamo field generated in the convective core.

Hence, dynamo action could also take place in the small inner convective cores of some hot stars (Stello et al. 2016). It is argued that surface fields could be due to the emergence of magnetic field blobs produced by a powerful convective dynamo in the innermost core (Parker 1975; Charbonneau & MacGregor 2001). However, the time required for this dynamo field to reach the stellar surface may be longer than the lifetime of the star (Moss 1989; MacGregor & Cassinelli 2003), unless very thin magnetic tubes could be generated. Moreover, in radiative interiors only magnetic fields much stronger than the equipartition value in the innermost convective core are able to be carried out to the stellar surface, which challenges the core-dynamo model (MacDonald & Mullan 2004). Interactions between a fossil field and a core dynamo are also possible, leading to a superequipartition state in the convective core (Featherstone et al. 2009).

In early-type O and B stars, a sub-surface convective layer may exist and a dynamo could develop in this layer (Cantiello & Braithwaite 2011). This mechanism produces magnetic fields of strength between 5 and 50 G, rather small scale and time-dependent, while the observed fields are mainly dipolar, stable over time and of much stronger amplitude. In intermediate-mass stars (smaller than $8\,M_{\odot}$), such as Vega and Sirius, sub-surface convective layers are also expected (Cantiello & Braithwaite 2011), although being of different physical nature. Nevertheless, the dynamo action in such thin layers is unlikely to sustain magnetic fields of large-enough length scales to be detectable (Kochukhov & Sudnik 2013).

Another hypothesis relies on a dynamo action in the radiative envelope. Indeed, differential rotation can trigger various instabilities which lead to dynamo action, as shown by self-consistent numerical simulations (MacDonald & Mullan 2004; Guervilly & Cardin 2010; Arlt & Rüdiger 2011b; Marcotte & Gissinger 2016). Several instabilities are likely to occur in stellar interiors (Spruit 1999). Dynamo cycles (of the $\alpha\Omega$-type), based on flux-tube instabilities (e.g. Ferriz-Mas et al. 1994; Zhang et al. 2003), the magnetorotational instability (Balbus & Hawley 1991; Mizerski & Lyra 2012) or the pinch-type Tayler instability (Tayler 1973; Markey & Tayler 1973; Pitts & Tayler 1985) have been proposed. In stably stratified envelopes, a pinch-type instability is expected to be the first to occur (Spruit 1999). Thus, recent theoretical and experimental works (Gellert et al. 2011; Seilmayer et al. 2012; Weber et al. 2015) focused on the Tayler instability in fluids with low magnetic Prandtl number, but yielded contradictory results. The dynamo capability of the Tayler instability in radiative envelopes was considered by Spruit (2002) and Braithwaite (2006). This mechanism is conceptually similar to the one driven by the magnetorotational instability (e.g. Jouve et al. 2015). An initial axisymmetric poloidal seed field is transformed by the Ω effect into an axisymmetric toroidal field. Then, a magnetic instability in the toroidal field develops to generate non-axisymmetric field components. To close the dynamo loop, a regeneration of either an axisymmetric toroidal (Spruit 2002) or poloidal field (Braithwaite 2006) is invoked. Braithwaite (2006) conducted numerical simulations, which seem to validate the dynamo mechanism in stellar stratified interiors. This dynamo mechanism has been criticized by Zahn et al. (2007). They used numerical simulations that did not lead to dynamo action. However, these simulations considered high magnetic diffusivity, yielding a differential rotation in these simulations below the threshold for dynamo action (Braithwaite & Spruit 2017). Later, Arlt & Rüdiger (2011a) and Szklarski & Arlt (2013) observed dynamo action in numerical simulations. Finally, Jouve et al. (2015) found that the magnetorotational instability seems favoured at the expense of the Tayler instability in differentially rotating, incompressible stars.

Undoubtedly, clarifying the relevance of these dynamo mechanisms in more realistic models of stably stratified stars deserves future work. Observational tests should play an essential role. In particular, a correlation between the stellar rotation and the magnetic field properties should exist (e.g. Potter et al. 2012), but this is not observed (Hubrig et al. 2006; Mathys 2017). Then, in all scenarios based on differential rotation, an energy source for that differential rotation needs to be identified. Indeed, the toroidal field is produced by shearing the poloidal field and it draws its energy from the differential rotation. As a result, this mechanism could only operate as long as a differential rotation exists. However, magnetohydrodynamic effects tend to weaken the initial differential rotation, which may be provided by the stellar contraction occurring during the PMS phase, through dissipative processes (Arlt et al. 2003; Jouve et al. 2015). Ultimately, the latter effects weaken the energy source of the dynamo action. Strong field strengths at the stellar surface are also expected to warrant a uniformly rotating radiative envelope (Spruit 1999), for instance in B3.5V star HD 43317 (Buysschaert et al. 2017).

Tidal forcing is another possible mechanism in radiative stars, as long as stars host non-synchronized orbital companions. Indeed, tidally deformed fluid bodies are prone to the tidal instability (e.g. Kerswell 2002; Cébron et al. 2013; Barker et al. 2016; Vidal & Cébron 2017). The latter is a hydrodynamic instability of elliptical streamlines that excites inertial waves through parametric resonance. The non-linear outcome of the tidal instability could lead to space-filling turbulence (e.g. Barker & Lithwick 2013a,b; Barker 2016; Le Reun et al. 2017). It has been proposed that the tidal instability is of significant importance for tidal dissipation in binary systems (Rieutord 2004; Le Bars et al. 2010) and for angular

momentum transport in accretion discs (Goodman 1993). The dynamo capability of the tidal instability has been confirmed by numerical simulations (Barker & Lithwick 2013b; Cébron & Hollerbach 2014). Apart from dynamo action in hot stars, it has also been shown that a Hot Jupiter companion is responsible for the stellar activity enhancement of low-mass HD 179949 star (Fares et al. 2012). The role of the close-in massive planet in the short activity cycle of the star τ Bootis has also been suggested (Fares et al. 2009). Finally, tides might also lead to a resonant excitation of helical oscillations driven by the Tayler instability, suggesting a possible planetary synchronization of the solar dynamo (Stefani et al. 2016).

1.3 Motivations

On one hand, the hydrodynamic non-linear regime of the tidal instability has been studied in unstratified fluids by Cébron et al. (2010a), Barker & Lithwick (2013a), Barker (2016), and Grannan et al. (2016). The tidal instability can induce a magnetic field (Lacaze et al. 2006; Herreman et al. 2010), paving the way to dynamos as suggested by Mizerski et al. (2012). Its dynamo capability has been proved by local (Barker & Lithwick 2013b) and global numerical simulations (Cébron & Hollerbach 2014). On the other hand, the non-linear regime of the tidal instability in stably stratified fluids has been studied by Cébron et al. (2010b), but only for a very limited range of parameters. It remains unclear how the tidal instability is modified in stably stratified layers. Consequently, the main purpose of this numerical study is to investigate the non-linear outcome of the tidal instability in stably stratified fluids and then to assess its dynamo capability.

Numerical simulations of the tidal instability are difficult to carry out. The parameter space of stellar interiors is impossible to simulate with the available computational resources. To simulate more realistic configurations we may use local models. Local simulations of the tidal instability in periodic boxes (e.g. Barker & Lithwick 2013a,b; Le Reun et al. 2017) indeed give quantitative predictions in good agreement with global simulations (Cébron et al. 2010a; Cébron & Hollerbach 2014; Barker et al. 2016; Barker 2016) and laboratory observations (Le Bars et al. 2010; Grannan et al. 2016). However, it is unclear whether possible small-scale dynamos obtained with local models could lead to large-scale magnetic fields in stellar interiors.

Here, we use global numerical simulations to study the tidal instability and its coupling to a magnetic field. In such simulations, the internal magnetic field matches a potential field outside the tidally deformed domain – such as a triaxial ellipsoid. This is a source of great mathematical complexity in non-spherical geometries (e.g. Wu & Roberts 2009). Existing numerical codes capable of handling ellipsoidal boundaries – such as codes based on finite elements (Cébron et al. 2010b, 2012a), spectral finite elements (Favier et al. 2015; Barker 2016) or finite volumes (Vantieghem et al. 2015) – approximate this magnetic boundary condition at the cost of both low accuracy and slow execution. However, high performance is crucial to try to reach the low viscosity limit relevant for astrophysical bodies. We choose to perform proof-of-principle numerical simulations in a spherical container. By considering a sphere, we benefit from the efficiency and accuracy of spectral codes relying on spherical harmonics (Schaeffer 2013; Matsui et al. 2016). We extend the method proposed by Cébron & Hollerbach (2014) to handle stratification. We assume that the fluid is subjected to a non-conservative body force sustaining an analytically designed tidally driven flow, valid in spherical geometry and satisfying the various constraints (including the viscous boundary condition). This flow is then prescribed in the code, and we consider the departure from the basic state.

The paper is organized as follows. In Section 2, we present the mathematical and numerical formulations of the problem. Numerical results are presented and discussed in depth in Section 3. Then, we extrapolate our results to stellar interiors in Section 4. Section 5 ends the paper with a discussion and perspectives.

2 DESCRIPTION OF THE PROBLEM

2.1 Governing equations

We model tides in a rotating fluid sphere of radius R_*. We consider a Newtonian fluid of uniform kinematic viscosity ν, thermal diffusivity κ, and magnetic diffusivity $\eta = 1/(\mu_0\sigma_e)$, where σ_e is the electrical conductivity and μ_0 the magnetic permeability of free space. The fluid is rotating with the spin–spin angular velocity $\Omega_s\widehat{\boldsymbol{z}}$ along the vertical axis. We consider the variations of density only in the buoyancy force, using the Boussinesq approximation (Spiegel & Veronis 1960). The density ρ is given by the non-barotropic equation of state

$$\rho = \rho_* \left[1 - \alpha(T - T_*)\right], \tag{1}$$

with α the coefficient of thermal expansion, (ρ_*, T_*) typical density and temperature and T the departure of the temperature field from the adiabatic temperature profile. In the Boussinesq framework, the fluid is stratified under the gravity field $\boldsymbol{g} = -\nabla\Phi_0$, with Φ_0 a prescribed gravitational potential. We choose R_* as unit of length, Ω_s^{-1} as unit of time, $\Omega_s^2 R_*/(\alpha g_0)$ as unit of temperature T, where g_0 is the gravitational acceleration at the stellar surface, and $R_*\Omega_s\sqrt{\mu_0\rho_*}$ as unit of magnetic field $\boldsymbol{B}$. We introduce the dimensionless Ekman number $Ek = \nu/(\Omega_s R_*^2)$, the Prandtl number $Pr = \nu/\kappa$, and the magnetic Prandtl number $Pm = \nu/\eta$. To quantify the stratification, we introduce the dimensionless (local) Brunt–Väisälä frequency $N(\boldsymbol{r})$ defined by (Friedlander & Siegmann 1982)

$$N^2(\boldsymbol{r}) = -\alpha\boldsymbol{g}\cdot\nabla T, \tag{2}$$

The fluid is stably stratified if $N^2 > 0$.

We work in spherical coordinates (r, θ, ϕ). We expand in the inertial frame the velocity field and the temperature as perturbations $(\boldsymbol{u}, \Theta, \boldsymbol{B})$ around a steady tidally driven basic state $(\boldsymbol{U}_0, T_0, \boldsymbol{0})$. In the inertial frame, the dimensionless non-ideal, non-linear magnetohydrodynamic equations are

$$\frac{\partial\boldsymbol{u}}{\partial t} = -(\boldsymbol{u}\cdot\nabla)\boldsymbol{U}_0 - (\boldsymbol{U}_0\cdot\nabla)\boldsymbol{u} - (\boldsymbol{u}\cdot\nabla)\boldsymbol{u} - \nabla p + Ek\,\nabla^2\boldsymbol{u} - \Theta\,\boldsymbol{g} + (\nabla\times\boldsymbol{B})\times\boldsymbol{B}, \tag{3a}$$

$$\frac{\partial\Theta}{\partial t} = -(\boldsymbol{U}_0\cdot\nabla)\Theta - (\boldsymbol{u}\cdot\nabla)T_0 - (\boldsymbol{u}\cdot\nabla)\Theta + \frac{Ek}{Pr}\nabla^2\Theta, \tag{3b}$$

$$\frac{\partial\boldsymbol{B}}{\partial t} = \nabla\times(\boldsymbol{U}_0\times\boldsymbol{B}) + \nabla\times(\boldsymbol{u}\times\boldsymbol{B}) + \frac{Ek}{Pm}\nabla^2\boldsymbol{B}, \tag{3c}$$

$$\nabla\cdot\boldsymbol{u} = 0, \quad \nabla\cdot\boldsymbol{B} = 0, \tag{3d}$$

with p the modified pressure, ensuring the incompressibility of the dynamics. For hydrodynamic computations, the Lorentz force $(\nabla\times\boldsymbol{B})\times\boldsymbol{B}$ is removed. Equations (3) are supplemented with appropriate boundary conditions. The velocity field satisfies the stress-free boundary condition

$$\boldsymbol{u}\cdot\boldsymbol{n} = 0, \quad \boldsymbol{n}\times\left[\boldsymbol{n}\cdot(\nabla\boldsymbol{u} + (\nabla\boldsymbol{u})^T)\right] = \boldsymbol{0}, \tag{4}$$

where $\boldsymbol{n}$ is the unit radial vector. Following Cébron & Hollerbach (2014), we impose a zero-angular momentum for $\boldsymbol{u}$. We also assume a fixed temperature $\Theta = 0$ at the boundary. Finally, the external region ($r > 1$) is assumed to be electrically insulating. Thus, the magnetic field matches a potential field at the boundary.

The governing equations (3) are solved with the open-source parallel XSHELLS code (e.g. Schaeffer et al. 2017). It has been validated against standard benchmarks (Marti et al. 2014; Matsui et al. 2016). It uses second-order finite differences in radius and pseudo-spectral spherical harmonic expansion, handled efficiently by the free SHTNS library (Schaeffer 2013). The time-stepping scheme is of second order in time, and treats the diffusive terms implicitly, while the non-linear and Coriolis terms are handled explicitly. For this study, we have extended the XSHELLS code to handle arbitrary basic state fields.

All simulations have been performed at $Ek = 10^{-4}$, $Pr = 1$ with various N_0/Ω_s and Pm. The spatial discretization uses $N_r = 224$ radial points, $l_{max} = 128$ spherical harmonic degrees, and $m_{max} = 100$ azimuthal wavenumbers. We made sure that our simulations are numerically converged by varying the spatial resolution.

2.2 Tidal basic state

The disturbing tidal potential perturbs the spin solid-body rotation to generate a flow with elliptical streamlines, known as the equilibrium tide (e.g. Zahn 1966; Remus et al. 2012). A difficulty is to numerically establish the equilibrium tide in spherical geometry. Following Favier et al. (2014), we can impose numerically a non-zero radial flow, or similarly decompose the flow into non-wave-like and wave-like parts (Ogilvie 2005; Rieutord & Valdettaro 2010; Ogilvie 2013; Lin & Ogilvie 2017). However, the relevance of these methods are elusive for dynamo computations, because the fluid suddenly becomes insulating when crossing the spherical boundary.

We assume that the fluid is subjected to a non-conservative body force $\boldsymbol{f}$ and heat source term $\mathcal{Q}$. They aim at deforming the axisymmetry (mimicking tidal effects), yielding the basic flow $\boldsymbol{U}_0$ and the basic temperature T_0. As in the non-wave-like decomposition (e.g. Rieutord & Valdettaro 2010), the body force $\boldsymbol{f}$ is vortical (Cébron & Hollerbach 2014), i.e. $\nabla \times \boldsymbol{f} \neq \boldsymbol{0}$. This is a necessary condition to deform the circular streamlines of the solid-body rotation into elliptical ones in incompressible fluids.

Instead of directly prescribing $\boldsymbol{f}$ (Cébron & Hollerbach 2014) and $\mathcal{Q}$ in the governing equations (5a), we prescribe an analytical basic flow $\boldsymbol{U}_0$ and temperature T_0. Indeed, imposing $(\boldsymbol{U}_0, T_0)$ is computationally more efficient, because we solve the departure from the basic state. Moreover, the imposed tidally driven basic state satisfies the various boundary constraints (including the viscous boundary condition). The imposed analytical basic state $(\boldsymbol{U}_0, T_0)$, is an exact steady solution of the primitive equations in the inertial frame

$$(\boldsymbol{U}_0 \cdot \nabla)\boldsymbol{U}_0 = -T_0\,\boldsymbol{g} - \nabla P_0 + Ek\,\nabla^2 \boldsymbol{U}_0 + \boldsymbol{f}, \tag{5a}$$

$$(\boldsymbol{U}_0 \cdot \nabla)\, T_0 = \frac{Ek}{Pr}\nabla^2 T_0 + \mathcal{Q}, \tag{5b}$$

$$\nabla \cdot \boldsymbol{U}_0 = 0. \tag{5c}$$

The body force $\boldsymbol{f}$ and the heat source term $\mathcal{Q}$ can be analytically computed from equations (5). Their mathematical expressions are rather lengthy and so they are not provided here.

The basic state depends solely on a stream function Ψ_0 as follows. The disturbing tidal potential generates an elliptical flow of azimuthal wavenumber $m = 2$, superimposed on the spin solid-body rotation ($m = 0$). For simplicity, we consider a dimensionless basic flow of the form

$$\boldsymbol{U}_0(\boldsymbol{r}) = \nabla \times [\Psi_0(\boldsymbol{r})\widehat{\boldsymbol{z}}], \tag{6}$$

where $\Psi_0(\boldsymbol{r})$ is a stream function given by

$$\Psi_0(\boldsymbol{r}) = -\frac{r^2}{2} + \epsilon\, f(r,\theta)\cos(2\phi), \tag{7}$$

with ϵ the maximum equatorial ellipticity and $f(r, \theta) \leq 1$ the local ellipticity profile. The effective ellipticity is $\beta(r, \theta) = \epsilon f(r, \theta)$. The latter profile is built to ensure that the basic flow $\boldsymbol{U}_0$ satisfies the stress-free boundary condition (4). It is also constrained by a regularity condition at the centre (Lewis & Bellan 1990). After little algebra it reads

$$f(r,\theta) = \frac{256}{9} r^2 \left(\frac{1}{3} - r^2 + r^4 - \frac{1}{3} r^6\right) \frac{r^2 \sin^2\theta}{2}. \tag{8}$$

The basic flow $\boldsymbol{U}_0$ satisfies the stress-free boundary condition (4). It is an approximation of the equilibrium tide (Zahn 1966; Remus et al. 2012).

Then, we choose a background temperature profile of the form $T_0 = N_0^2/\Omega_s^2\,\Phi_0$, where N_0 is the dimensional Brunt–Väisälä frequency at the outer boundary ($N_0^2 \geq 0$). It has a fixed temperature at the boundary and cancels out the baroclinic instability, as a result of $\nabla T_0 \times \boldsymbol{g} = \boldsymbol{0}$. Thus, we ensure a barotropic basic state. We further assume a linear dependence between the imposed gravitational potential Φ_0 and the stream function, i.e. $\Phi_0 = -\Psi_0$. Therefore, isotherms in the basic state coincide with streamlines. With this choice the imposed gravitational potential is constant at the outer spherical boundary ($r = 1$).

Finally, the tidally driven basic state (7) does not take into account the rotation of the tidal ellipticity due to the companion's orbital motion. Indeed, the rotation of the tidal strain does not modify the underlying physical mechanism of the tidal instability (Le Bars et al. 2010; Cébron & Hollerbach 2014). In the non-rotating orbital case, the zero angular momentum condition imposed for $\boldsymbol{u}$ is in agreement with the conservation of the angular momentum of the star.

Our basic state is illustrated in Fig. 1 for a given set of parameters. The effective tidal ellipticity equals its maximum value ϵ at $r = 0.5$ and decreases towards the centre and the outer boundary where it vanishes. As a consequence, azimuthal averages of T_0, $\boldsymbol{g}$, and of the background Brunt–Väisälä frequency almost vary linearly in radius, as observed in Fig. 1(b). Hence, our basic stratification is almost spherically symmetric, which is expected for rotating stars.

3 NUMERICAL RESULTS

3.1 Hydrodynamic regime

The magnetic field is kept at zero in equations (3) to study purely hydrodynamic instabilities of the equilibrium tide $\boldsymbol{U}_0$. When the maximum tidal ellipticity ϵ is greater than a critical value ($\epsilon_c = 0.054$ in the neutral case $N_0 = 0$), the basic flow $\boldsymbol{U}_0$ is unstable. The perturbation flow $\boldsymbol{u}$ grows exponentially and then saturates non-linearly. Perturbation velocities $\boldsymbol{u}$ of larger amplitudes are obtained for larger ϵ, but we also want to keep ϵ small enough for the basic state to remain close to a solid-body rotation. Consequently, we choose $\epsilon = 0.2 (\simeq 4\epsilon_c)$ to survey the parameter space in the following.

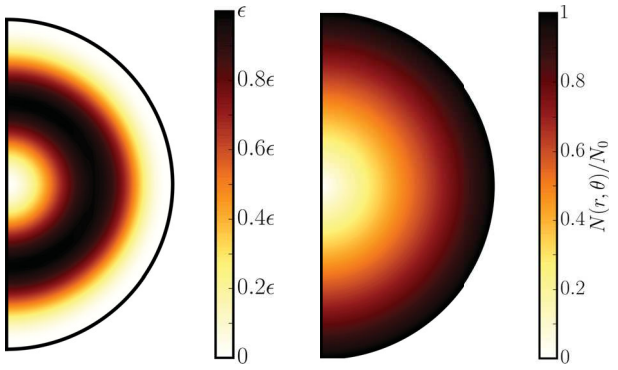

(a) Ellipticity (b) Brunt-Väisälä frequency

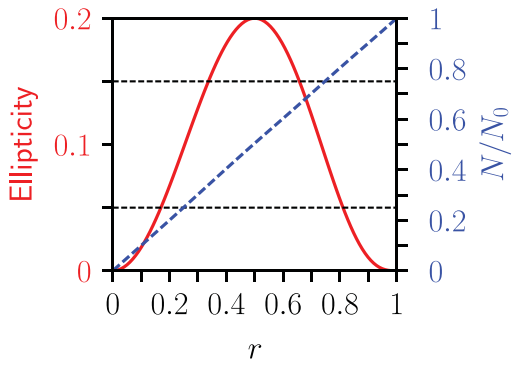

(c) Ellipticity and Brunt-Väisälä frequency versus radius

Figure 1. (a) Ellipticity $\epsilon f(r, \theta)$ in a meridional plane, computed at $\epsilon = 0.2$. (b) Normalized Brunt–Väisälä frequency of the basic state $N(r, \theta)/N_0$ in the meridional plane $\phi = 0$. (c) Equatorial ellipticity $\epsilon f(r, \pi/2)$ and $N(r, \theta)/N_0$ are shown as solid and dashed lines, respectively. Horizontal dashed lines represent the critical ellipticity $\epsilon_c = 0.05$ and 0.15, for $N_0/\Omega_s \ll 1$ and $N_0/\Omega_s \simeq 2$, respectively.

The nature of the hydrodynamic instability is revealed in the linear growth phase. If the perturbation flow satisfies the global resonance condition (Kerswell 2002)

$$|m_1 - m_2| = 2, \tag{9}$$

where (m_1, m_2) is the azimuthal wavenumber pair of the inertial modes (i.e. the eigenmodes of a rotating cavity) resonating with the tidal basic flow ($m = 2$), then the instability is a tidal instability. In Fig. 2(a), we show the most energetic wavenumber pair (m_1, m_2) excited in the exponential growth as function of N_0/Ω_s. All pairs satisfy the condition (9), hence a tidal instability is always excited in the explored range of stratification ($0 \leq N_0/\Omega_s \leq 100$). It is an equatorially symmetric flow, appearing first at radius $r = 0.5$ where the ellipticity is maximum (see Fig. 1), which then spreads out in the bulk. When $N_0/\Omega_s \lesssim 1$, the pair (2, 4) is excited and the typical growth rate is $\sigma/\epsilon \simeq 10^{-1}$ irrespective of the value of N_0. It yields typical time-scales for the instability to grow between 30 ky and 3 My for typical stellar interiors with $\epsilon \in [10^{-8}, 10^{-6}]$ and a one-day spin period. The flow oscillates at the angular frequency $\omega \leq 2$, suggesting that the parametric resonance involves inertial modes. When $1 \lesssim N_0/\Omega_s \leq 2$, we observe different pairs of unstable modes and the growth rates of the tidal instability are lower. In this range, the typical frequencies of inertial modes and internal gravity modes are similar. As a result of the interplay between the two effects of same order of magnitude, a complex pattern of unstable modes is expected. The most unstable pair (2, 4) at $N_0 = 0$ is first replaced by

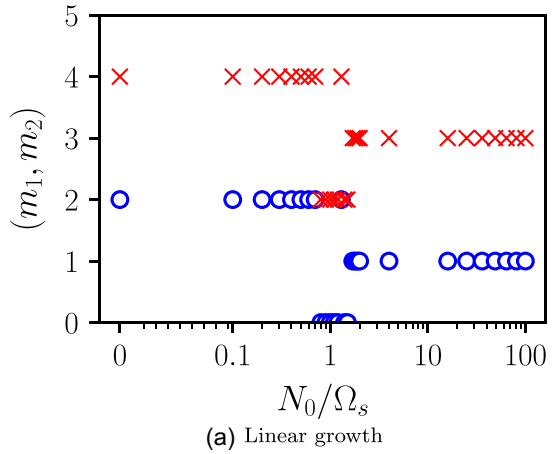

(a) Linear growth

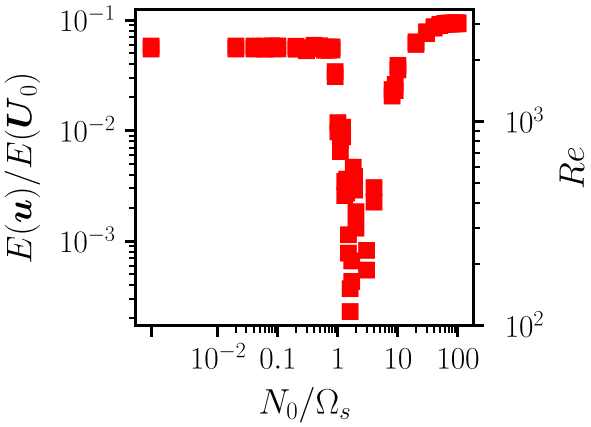

(b) Nonlinear saturation

Figure 2. Survey of hydrodynamic simulation of the tidal instability at $Ek = 10^{-4}$, $Pr = 1$, and $\epsilon = 0.2$ for varying N_0/Ω_s. (a) Pair of the most rapidly growing wavenumbers m_1 (circles) and m_2 (crosses) excited in the exponential growth. (b) Volume average kinetic energy of the perturbation $E(\boldsymbol{u})$ normalized by the kinetic energy of the basic flow $E(\boldsymbol{U}_0)$ and Reynolds number Re.

the pair (0, 2) when $0.8 \leq N_0 \leq 1.5$ and then by the pair (1, 3). When $N_0/\Omega_s \geq 2$, the buoyancy force becomes of primary importance and the stratification is then expected to be always stabilizing (Miyazaki 1993). However, we observe that the tidal instability is not inhibited. Furthermore, the hydrodynamic growth rates are slightly enhanced by a large stratification, with $\sigma/\epsilon \simeq 5 \times 10^{-1}$. It yields dimensional time-scales for the instability to growth of order 5 ky–0.5 My for typical stellar interiors, with $\epsilon \in [10^{-8}, 10^{-6}]$ and a one-day spin period.

Finally, the observed pairs (m_1, m_2) depend on the diffusion in our simulations. In asymptotic regime of low diffusion ($Ek \to 0$), we expect the excitation of a wider range of pairs (m_1, m_2), possibly with large azimuthal numbers, leading to wave turbulence (Le Reun et al. 2017).

To quantify the non-linear outcome of the tidal instability, we compute in Fig. 2(b) the kinetic energy of the perturbation

$$E(\boldsymbol{u}) = \int_V \frac{|\boldsymbol{u}|^2}{2} \mathrm{d}V, \tag{10}$$

(with $V = 4\pi/3$, the dimensionless volume of the sphere), as a function of N_0/Ω_s. We also introduce the Reynolds number $Re = Ro/Ek$ with $Ro = \sqrt{E(\boldsymbol{u})/E(\boldsymbol{U}_0)}$ the Rossby number and $E(\boldsymbol{U}_0)$ the

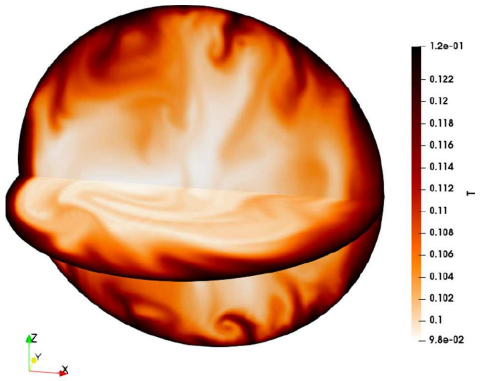

(a) $N_0/\Omega_s = 0.5$

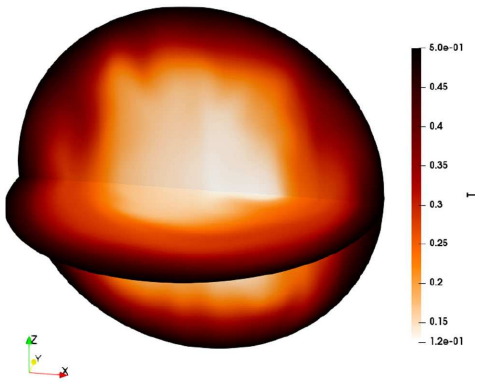

(b) $N_0/\Omega_s = 1$

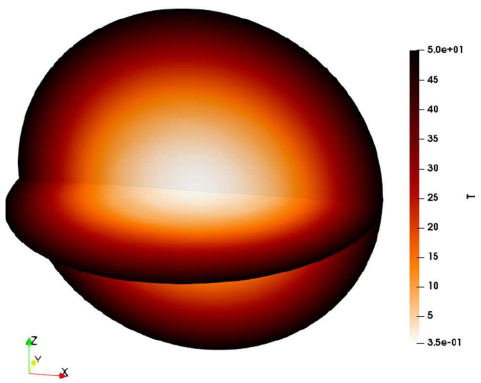

(c) $N_0/\Omega_s = 10$

Figure 3. Three-dimensional views of the total temperature $T = T_0 + \Theta$ in the non-linear regime of the tidal instability. Surfaces of constant T are shown in the equatorial plane and in a meridional plane. Simulations at $Ek = 10^{-4}$, $Pr = 1$, and $\epsilon = 0.2$.

kinetic energy of the global rotation. Three regimes are observed in the simulations. Illustrative three-dimensional snapshots of the total temperature field $T = T_0 + \Theta$ in these regimes are shown in Fig. 3. When $0 \leq N_0/\Omega_s \lesssim 1$, the tidal instability flow is immune to the stable stratification, as in the linear growth phase. The instability is almost four times critical in this range ($\epsilon/\epsilon_c \simeq 3.7$) and the typical Reynolds number is $Re = 2000$. The flow has a kinetic energy representing about 5 per cent of the kinetic energy of the global rotation, consistent with the expected dimensional amplitude $\epsilon\,\Omega_s R_*$ in the neutral ($N_0 = 0$) case (Barker & Lithwick 2013a; Grannan et al. 2016; Barker 2016). In Fig. 3(a), the stratification seems to be well mixed and eroded in the bulk (compare with Fig. 1b), below a thermal boundary layer (due to our thermal boundary condition). We note that the fluid is no longer barotropic, since the instantaneous isolines of T do not coincide with the isopotentials anymore.

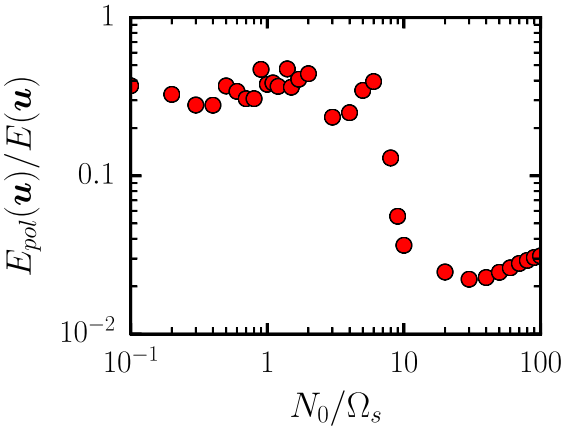

Figure 4. Instantaneous fraction of poloidal to total kinetic energy $E_{\rm pol}(\boldsymbol{u})/E(\boldsymbol{u})$, denoted $F_{\rm pol}$, as a function of N_0/Ω_s. Simulations at $Ek = 10^{-4}$, $Pr = 1$, and $\epsilon = 0.2$

When $1 \lesssim N_0/\Omega_s \leq 2$, we observe a collapse of the kinetic energy. For these stratifications, the interplay between inertial and internal waves reduces the saturation amplitude of the tidal instability. As a consequence, we observe also a reduction in the mixing in Fig. 3(b). The collapse when $1 \lesssim N_0/\Omega_s \leq 2$ is due to a variation of ϵ_c there, likely due to diffusion effects (see Appendix). This effect is not expected in radiative stellar interiors, characterized by much lower diffusivities. Finally, when $N_0/\Omega_s \geq 2$, the strong stratifications do not prevent the tidal instability. Instead the instability has an even larger amplitude, with a typical Reynolds number $Re = 3000$ and a kinetic energy representing still about 5 per cent of the kinetic energy of the basic flow, see Fig. 2(b). This translates to a dimensional flow amplitude $\epsilon\,\Omega_s R_*$ regardless of the strong stratification. The total temperature field displayed in Fig. 3(c) seems however hardly disturbed by the instability, implying that the motions are mostly confined to spherical shells with almost no radial component. This is confirmed by the ratio $F_{\rm pol}$ of poloidal kinetic energy to the total kinetic energy, shown in Fig. 4. For $N_0/\Omega_s \leq 1$, $F_{\rm pol}$ mostly lies between 0.3 and 0.4. When $N_0/\Omega_s \geq 1$, first $F_{\rm pol}$ seems to take values between 0.1 and 0.5, before dropping below 0.05 when the stratification is further increased in the range $N_0/\Omega \geq 10$. These low values of the poloidal kinetic energy show that the flow has consistently a weak radial component when $N_0/\Omega_s \geq 10$.

3.2 Kinematic dynamos

We remove the Lorentz force $(\nabla \times \boldsymbol{B}) \times \boldsymbol{B}$ from the momentum equation (3a) to investigate kinematic dynamos. In this problem, we assess the dynamo capability of the non-linear tidal motions, without a back reaction of the magnetic field on the flow. We introduce the magnetic Reynolds number

$$Rm = Pm\,Re, \tag{11}$$

with Re the Reynolds number previously introduced. If the structure of the tidal instability flow is suitable for dynamo action, Rm has a finite critical value Rm_c above which the dynamo process starts, characterized by the growth of a magnetic field. Equivalently, the dynamo threshold Rm_c is associated with a critical magnetic Prandtl number Pm_c for a fixed value of Ek.

We have considered several values of the magnetic Prandtl number ($1 \lesssim Pm \leq 5$), starting from random magnetic seeds, to

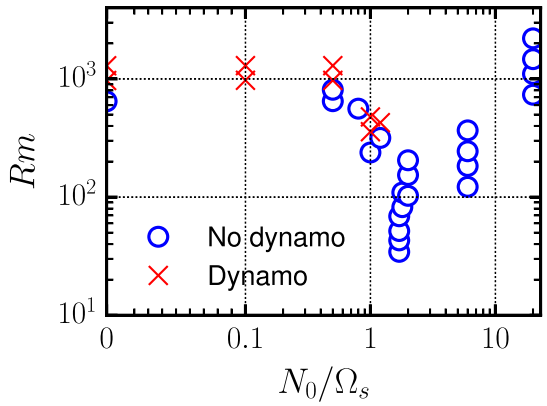

Figure 5. Survey of kinematic dynamos for varying N_0/Ω_s and Rm. Simulations at $Ek = 10^{-4}$, $Pr = 1$, and $\epsilon = 0.2$

determine Pm_c. We have checked that the laminar basic flow $\boldsymbol{U}_0$ is not dynamo capable for $Pm \leq 5$, but it does not preclude a laminar dynamo driven by the basic flow at higher Pm. To detect the onset of kinematic dynamo action, we monitor the time evolution of the mean magnetic energy density $E(\boldsymbol{B}) = \int_V |\boldsymbol{B}|^2/2\,\mathrm{d}V$ and deduce the growth rate σ_b by fitting with an exponential function. The kinematic dynamos we obtained are summarized in Fig. 5. Typical growth rates are $\sigma_b = \mathcal{O}(10^{-3})$.

Non-linear motions are always dynamo capable when $0 \leq N_0/\Omega_s \lesssim 1$, at least for $Pm \geq 1.5$ at $Ek = 10^{-4}$. This yields a typical dynamo threshold $Rm_c \simeq 3000$, a plausible value for dynamo action. This value is higher than the one obtained for precession-driven (Tilgner 2005; Goepfert & Tilgner 2016) and tidally driven (Cébron & Hollerbach 2014) dynamos in neutral fluids.

In the range $1 \lesssim N_0/\Omega_s \leq 1.3$, several dynamos are obtained with a smaller $Rm_c \simeq 1000$. In the range $1.3 \leq N_0/\Omega_s < 10$, no dynamo is obtained for the considered $Pm \leq 2$. This is because the saturated amplitude of the flow is weak ($Re \simeq 100$), as a result of a higher ϵ_c there, leading to a much lower supercriticality (see Appendix). Studying this region would require a more systematic parameter survey, and in particular lowering the diffusivities. This would require more computational power than we currently have at our disposal and this is left for a future study. For stronger stratifications ($N_0/\Omega_s \geq 10$) we found no dynamo, even for the most extreme case with $Rm \simeq 8000$. This suggests that the non-linear tidal flows in this range are not dynamo capable as a results of their spatial structure, even if the Reynolds number can be larger ($Re \leq 2000$). Indeed, the toroidal velocity theorem states that an incompressible flow without radial component (i.e. purely toroidal) cannot sustain a magnetic field (Bullard & Gellman 1954). This theorem is not invalidating when small non-radial motions are considered (Kaiser & Busse 2017). When $N_0 \gg \Omega_s$, although being of considerable amplitude, the tidally driven flow seems constrained by the stratification and leads to weak radial motions, see Fig. 3(b). This is a plausible explanation of the lack of dynamos for reasonable values of Rm at $N_0/\Omega_s > 10$.

3.3 Self-consistent dynamos

Now we take the Lorentz force into account in the momentum equation (3a) to compute self-consistent dynamos. We integrate the governing equations (3) over one dimensionless magnetic diffusive time $t_\eta = Pm/Ek$ to get reliable dynamo results. We use the saturated tidal flow as initial conditions for the velocity field. All the kinematic

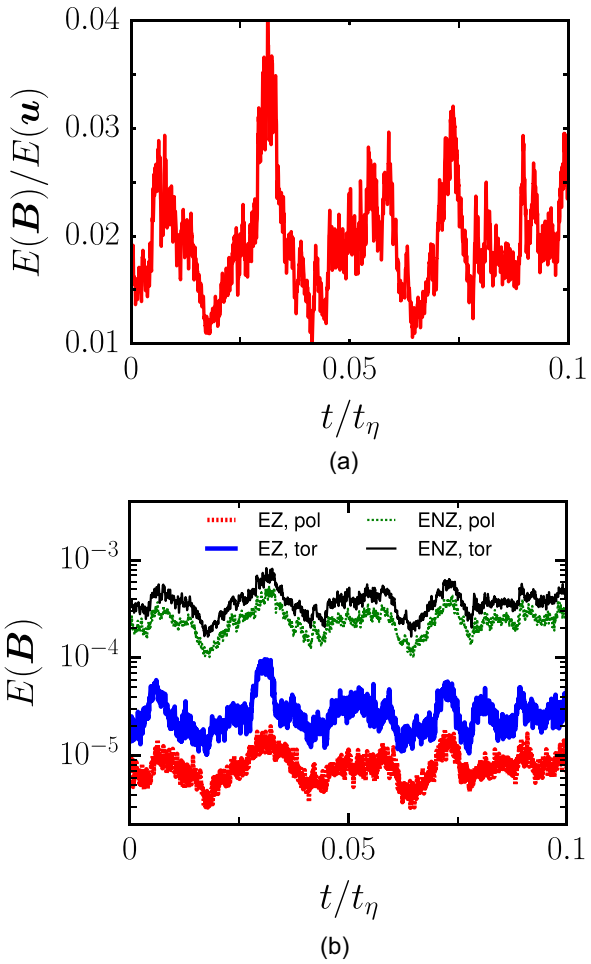

Figure 6. Self-consistent magnetic field in the saturation regime. Simulation at $Ek = 10^{-4}$, $Pr = 1$, $Pm = 2$, and $\epsilon = 0.2$. Only a small representative fraction of the dimensionless diffusive time $t_\eta = Pm/Ek$ is shown. (a) Ratio $E(\boldsymbol{B})/E(\boldsymbol{u})$. (b) Poloidal zonal ($m = 0$) energy (EZ, pol), toroidal zonal ($m = 0$) energy (EZ, tor), poloidal non-zonal ($m > 0$) (ENZ, pol) energy, and toroidal non-zonal ($m > 0$) energy (ENZ, tor) of the magnetic field.

dynamos obtained for $N_0/\Omega_s \lesssim 1$ give self-consistent dynamos. As in the hydrodynamic case, the simulations are qualitatively and quantitatively similar in the whole range $N_0/\Omega_s \lesssim 1$. We only provide a detailed analysis of the illustrative simulation performed at $N_0/\Omega_s = 0.5$, $\epsilon = 0.2$, and $Pm = 2$ (with $1.25 < Pm_c < 1.5$).

The magnetic energy, initially weak, is amplified and reaches values representing a small fraction of the kinetic energy of the flow driven by the tidal instability in Fig. 6(a). This fraction is about 0.01–0.02. Hence, the magnetic field does not reach a state of equipartition and the kinetic energy is therefore only slightly affected by the dynamo action. Note that these values are smaller than those obtained by Barker & Lithwick (2013b) in local simulations without buoyancy effects. However, with larger Rm, larger amplitude of the magnetic energy could be reached. The time evolution of the magnetic field seems to follow the time evolution of the velocity field (see Fig. 6). Magnetic energy has rapid oscillations, at frequency of the order of the spin rate, which are superimposed on longer period oscillations of small amplitudes. In Fig. 6(b), we observe that the zonal energy (i.e. axisymmetric $m = 0$ energy) is one order of magnitude smaller than the non-zonal energy (i.e. non-axisymmetric $m > 0$ energy). The magnetic field is also

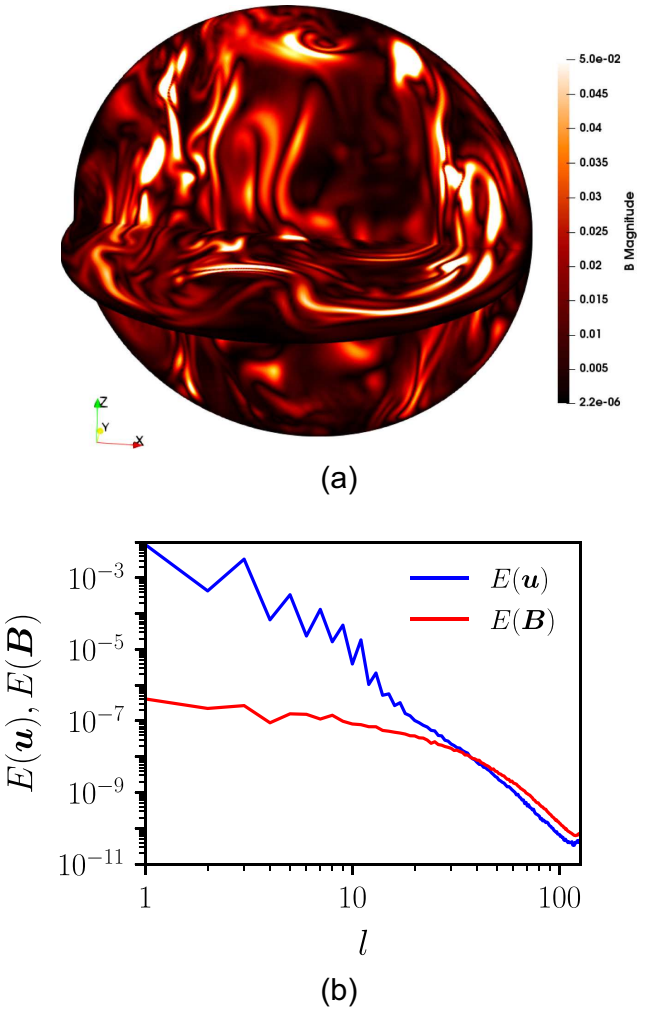

Figure 7. (a) Three-dimensional snapshot of the magnetic field magnitude $|\boldsymbol{B}|$ at a given time. The rotation axis is along z. (b) Time- and radius-averaged spectra of the magnetic energy as function of the spherical harmonic degree l. Simulation at $Ek = 10^{-4}$, $Pr = 1$, $Pm = 2$, and $\epsilon = 0.2$.

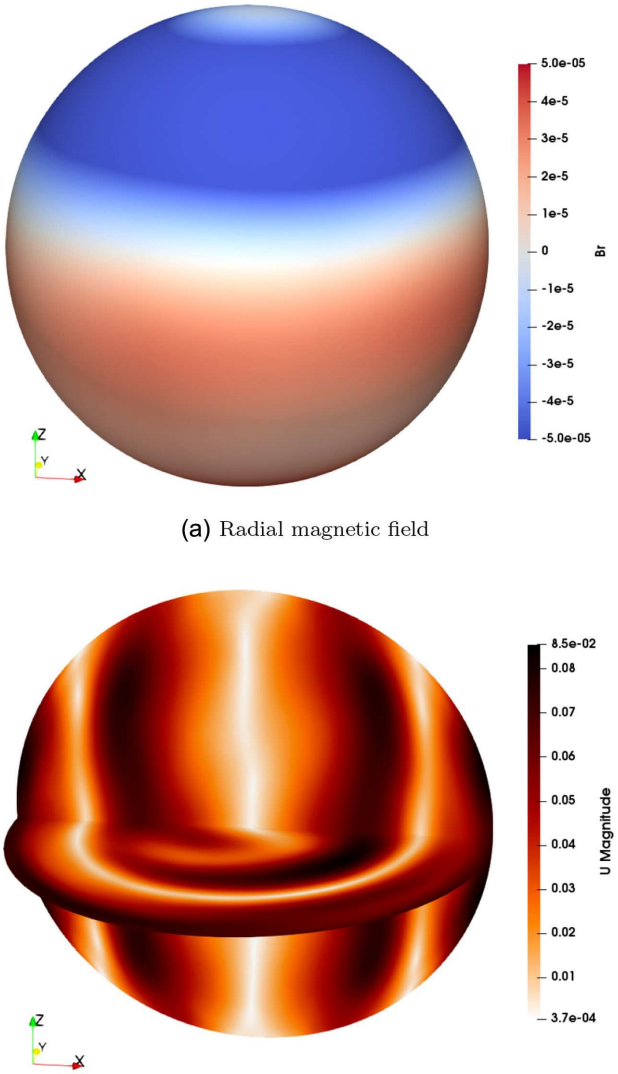

Figure 8. (a) Time-averaged radial magnetic field at the stellar surface and (b) time-averaged velocity magnitude in the equatorial plane and in a meridional plane. Simulations at $Ek = 10^{-4}$, $Pr = 1$, $Pm = 2$, and $\epsilon = 0.2$. Time-averaged fields computed from $t/t_\eta = 0$ to $t/t_\eta = 0.1$ in Fig. 6(b). In both figures, the spin axis is the vertical z-axis.

predominantly toroidal, as expected from stability considerations in non-barotropic stars (Akgün et al. 2013).

Because of the complex time evolution, straightforward visualizations of the instantaneous field are not illuminating. We show in Fig. 7(a) an instantaneous snapshot of the magnitude of the magnetic field. The field is of rather small scale. We observe similarities with the temperature field shown in Fig. 3(a). A description of the field morphology is provided by the time-averaged spectrum of the magnetic field in Fig. 7(b). The magnetic spectrum is dominated by components of spherical harmonic degrees $l \leq 10$. It is maximum for the dipolar component ($l = 1$) and then slowly decays with a power law $E(\boldsymbol{B}) \propto l^{-0.04}$. The time-averaged spectrum, as well as the instantaneous ones, are well resolved, proving that tidal motions are able to drive a dipole-dominated dynamo in a stably stratified layer.

We show in Fig. 8, the time-averaged magnetic field truncated at spherical harmonics degree $l = 5$, because higher degrees are not observed (e.g. Donati & Landstreet 2009; Fares et al. 2017). This time-averaged field is mostly dipolar ($l = 1$) and axisymmetric ($m = 0$). Non-axisymmetric components are averaged out because of the rapid spin. The time-averaged flow has a columnar structure aligned with the spin axis, as shown in Fig. 8(b). These spin-aligned structures are the global counterpart of the strong vortices almost invariant along the rotation axis and filling the periodic boxes of similar local simulations (Barker & Lithwick 2013a,b). These flows are expected in our stress-free computations with no viscous friction at the boundary (Livermore et al. 2016; Le Reun et al. 2017). The emergence of such spin-aligned large-scale vortices are also observed in rotating thermal convection (e.g. Guervilly et al. 2014) and have been shown to be dynamos (Guervilly et al. 2015).

3.4 Tidal mixing

We have shown that the tidal instability is dynamo capable in our simulations when $N_0/\Omega_s \lesssim 1$ with a dynamo threshold $Rm_c \simeq 3000$. For stronger stratifications ($N_0/\Omega_s \geq 10$), we did not find dynamo action up to $Rm \simeq 8000$ in the simulations. Indeed, dynamo action requires not only large Rm, but also adequate, sufficiently complex, flow structure (Kaiser & Busse 2017). Here, we suspect

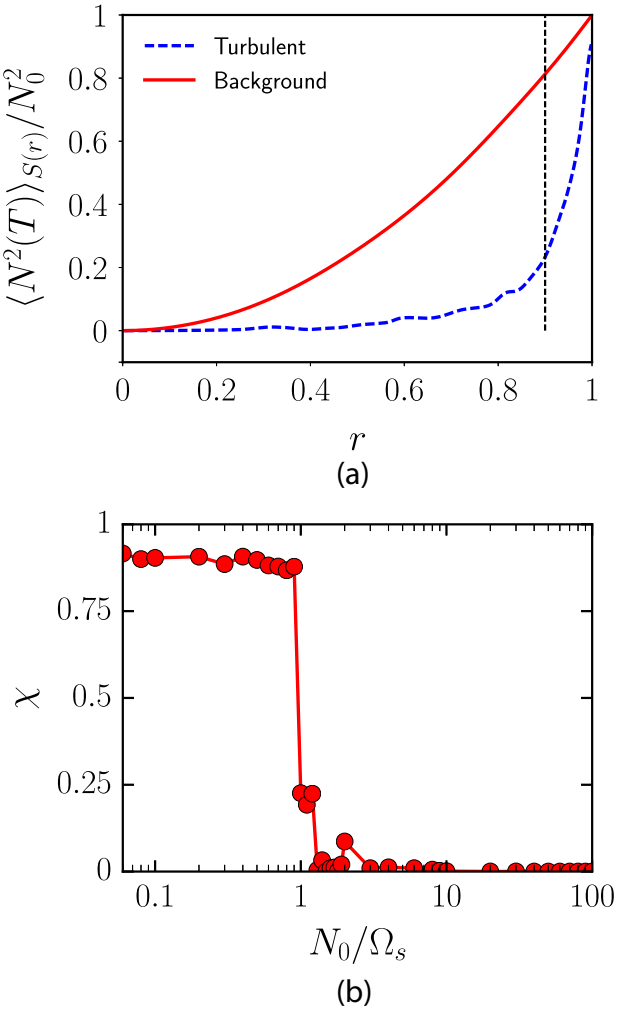

Figure 9. (a) Time average of the surface average ($l = 0$, $m = 0$) of the local Brunt–Väisälä frequency $\langle N^2(T)\rangle_{S(r)}$ as function of radius r. The vertical dashed line represents the beginning of the thermal boundary layer. (b) Efficiency of mixing χ for varying N_0/Ω_s. We fix $r_{tbl} = 0.9$ in formula (12). Simulations at $N_0/\Omega_s = 0.5$, $Ek = 10^{-4}$, $Pr = 1$, and $\epsilon = 0.2$.

the radial mixing induced by the tidal forcing to be important. Therefore, we now quantify the mixing induced by non-linear tidal motions.

As shown in Fig. 6(a), the magnetic energy is much smaller than the kinetic energy. Hence, the Lorentz force has little effect on the flow dynamics. To quantify how the background temperature T_0 is mixed by the tidal instability, we compute the time and spherical average of the local Brunt–Väisälä frequency $\langle N^2(T)\rangle_{S(r)}$, where $\langle.\rangle_{S(r)}$ is the average over the spherical surface $S(r)$ at radius r (i.e. $l = 0$ in spectral space). It is illustrated in Fig. 9(a) for the non-linear saturated regime of the simulation at $N_0/\Omega_s = 0.5$ and $\epsilon = 0.2$ (representative of the stratification $N_0/\Omega_s \lesssim 1$). The dashed line represents the background state. In the non-linear state (dashed line), the stratification is well mixed ($N^2(T) \simeq 0$) as suggested by Fig. 3(a), except near the outer boundary where a thermal boundary layer appears. This thermal boundary layer has a typical thickness of about 0.1 in our simulations.

To estimate the efficiency of the mixing, we compute a coefficient of mixing χ defined as follows

$$\chi = \left| 1 - \int_0^{r_{tbl}} \langle N^2(T)\rangle_{S(r)} \mathrm{d}r \left(\int_0^{r_{tbl}} \langle N^2(T_0)\rangle_{S(r)} \mathrm{d}r \right)^{-1} \right|, \qquad (12)$$

with $r_{tbl} = 0.9$, the bottom radius of the thermal boundary layer. If $\chi = 1$ then the stratification is entirely mixed (below the thermal boundary layer), while if $\chi = 0$ there is no mixing. Fig. 9(b) displays the evolution of χ with N_0/Ω_s. We find that the stratification is almost entirely mixed by the tidal instability (below the thermal boundary layer) when $N_0/\Omega_s \lesssim 1$. When $1 \lesssim N_0/\Omega_s \leq 2$, the mixing efficiency is strongly reduced. Then, we find that there is no mixing associated with the still vigorous tidal motions when $N_0/\Omega_s \geq 2$. We explain the observed dichotomy below and above $N_0/\Omega_s = 1$ based on the following simple arguments. A parametric resonance involving inertial modes is responsible for the tidal instability, which is almost insensitive to the stratification when $N_0/\Omega_s \lesssim 1$.

When $1 \lesssim N_0/\Omega_s \leq 2$, Coriolis and buoyancy forces are of the same order and thus a parametric instability involving inertia-gravity modes is responsible for the tidal instability. However, as shown in Appendix, the collapse in the kinetic energy in Fig. 2(b) when $1 \lesssim N_0/\Omega_s \leq 2$, responsible for the strong reduction of the mixing in Fig. 9(b), is due to a higher ϵ_c and to a lower super-criticality there. It is not expected to occur in stellar interiors in the asymptotic limit Ek, $Ek/Pr \to 0$ for these values of N_0/Ω_s. Thus, for smaller Ek, radial mixing is also expected in non-linear regimes.

Finally for stronger stratifications ($N_0/\Omega_s \geq 2$), the tidal instability generates motions mainly along spherical shells, as indirectly observed in the advection of the scalar temperature in Fig. 3(c). The tidal instability is linearly triggered near the locus of maximum ellipticity ($r = 0.5$) and generates there non-linear radial motions of short wavelengths (not shown). This is because the ellipticity is not homogeneous in our model (see Fig. 1), but in a ellipsoidal body (like a tidally deformed star), we expect it to appear everywhere. Non-linear motions are mostly toroidal motions of spherical coefficients ($l = 1, m = 1$). These motions seem similar to 'r modes'-like motions, which are the least-damped motions with stress-free boundary conditions (Rieutord 2001). The strong stratification inhibits radial flows and toroidal flows are favoured instead, unable to lead to efficient radial mixing.

4 ASTROPHYSICAL APPLICATIONS

To investigate the astrophysical importance of the tidal instability for stellar magnetism, we have to extrapolate our numerical results towards the parameter space of stellar interiors. We expect our numerical simulations to capture the dominant global scales of tidally driven non-linear motions. Indeed, there is a broad agreement with the observed magnetic pattern at the surface of many magnetic stars, showing a dominant dipolar field with possible smaller scales (Donati & Landstreet 2009). The instantaneous magnetic field and the potential field extrapolation (external field) of a model are shown in Fig. 10, truncating the magnetic spectrum at $l \leq 5$. Higher harmonics are not observed in astronomical data. The external potential field is still dominated by the dipolar component. Without scaling laws, we cannot extrapolate towards the parameter space of stellar interiors. Unfortunately, all available scaling laws have been developed for convective dynamos only (e.g. Christensen et al. 2009; Yadav & Christensen 2013; Yadav et al. 2013; Augustson et al. 2017) and cannot be safely applied to other forcings. Obtaining

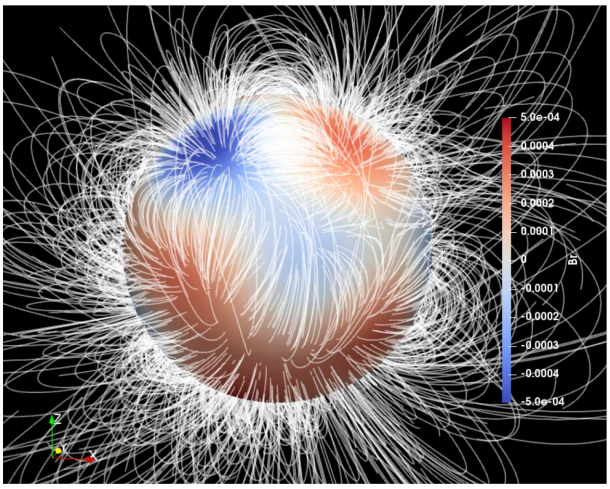

Figure 10. Potential field extrapolation of the instantaneous surface magnetic field (up to dimensionless radius $r = 2$). Simulations at $Ek = 10^{-4}$, $Pr = 1$, $Pm = 2$, and $\epsilon = 0.2$.

scaling laws would require to simulate lower viscosities, which are currently out of reach.

4.1 Tidal instability in stellar interiors

We carry out the extrapolation as follows. We consider a star of mass M_*, mean radius R_*, and equatorial ellipticity ϵ_*. The radiative zone is modelled as a stably stratified zone in the Boussinesq approximation. A tidal basic flow (equilibrium tide), induced by the disturbing tidal potential of an orbiting companion of mass m, is established within the radiative envelope. We consider only non-synchronized systems, where the spin angular velocity of the star $\Omega_s = 2\pi/P_s$ (with P_s the spin period) is not equal to the mean orbital rotation rate of the companion $\Omega_{orb} = 2\pi/P_{orb}$ (with P_{orb} the orbital period). For simplicity, we assume that the companion is moving on a circular orbit in the equatorial plane of the host star. The ellipticity ϵ_* is estimated from the static bulge theory (e.g. Cébron et al. 2012b; Vidal & Cébron 2017)

$$\epsilon_* = \frac{3}{2}\frac{m}{M_*}\left(\frac{R_*}{D}\right)^3, \tag{13}$$

with D the typical distance between the star and its orbital companion. An estimation of D can be obtained with Kepler's third law, yielding (Barker & Lithwick 2013b)

$$\epsilon_* = \frac{3}{2}\frac{m}{m+M_*}\left(\frac{\Omega_{orb}}{\Omega_{dyn}}\right)^2, \tag{14}$$

with the dynamical frequency $\Omega_{dyn} = \sqrt{GM_*/R_*^3}$ and G the gravitational constant.

The fastest growing mode of the tidal instability (in the asymptotic limit Ek, $Ek/Pr \to 0$) has the dimensional growth rate (e.g. Kerswell 2002)

$$\frac{\sigma}{|\Omega_s - \Omega_{orb}|} = \frac{(2\widetilde{\Omega}+3)^2}{16(1+\widetilde{\Omega})^2}\epsilon_*, \tag{15}$$

with $\widetilde{\Omega} = \Omega_{orb}/(\Omega_s - \Omega_{orb})$ the background rotation. Using astronomical quantities, formula (15) is rewritten as

$$\sigma = \frac{3}{2}\left|1 - \frac{\Omega_{orb}}{\Omega_s}\right|\frac{(2\widetilde{\Omega}+3)^2}{16(1+\widetilde{\Omega})^2}\frac{m}{D^3}\frac{R_*^3\Omega_s}{M_*} \leq 3\frac{m}{D^3}\frac{R_*^3\Omega_s}{M_*}. \tag{16}$$

The growth rate (16) is insensitive to the amplitude of the stratification N_0/Ω_s, as globally observed in our simulations (except for $1 \lesssim N_0/\Omega_s \leq 2$, see Appendix). The tidal instability is triggered for circular orbital configurations belonging to the allowable range $-1 \leq \Omega_{orb}/\Omega_s \leq 3$ (e.g. Le Bars et al. 2010). However, the tidal instability can be excited well outside this range for eccentric Kepler orbits (Vidal & Cébron 2017).

Based on our global simulations of the tidal instability, buoyancy effects do not influence amplitudes of tidal non-linear motions when $N_0/\Omega_s \leq 1$. For $N_0/\Omega_s \geq 10$, the tidal instability stays vigorous but the flow is constrained by the strong stratification resulting in weak radial motion, see Section 3.1 and Fig. 9. When $1 < N_0/\Omega_s < 10$, the lower amplitudes observed are due to a larger critical ellipticity, see Appendix. Therefore, as shown in Fig. 2(b), the tidal instability generates non-linear flows with a typical velocity magnitude (Barker & Lithwick 2013a,b; Grannan et al. 2016)

$$u \sim \epsilon_*|\Omega_s - \Omega_{orb}|R_*. \tag{17}$$

4.2 Prediction for the magnetic field strength

Dynamo action requires a large magnetic Reynolds number, i.e. $Rm > Rm_c$. This translates into a constraint on the magnetic diffusivity $\eta < uR_*/Rm_c$. Using the estimate (17) for u, we have

$$\eta < \epsilon_*|\Omega_s - \Omega_{orb}|R_*^2/Rm_c. \tag{18}$$

We assume a weak dependence of the dynamo threshold Rm_c on Pm_c when the diffusivities are decreased towards stellar values (i.e. $Ek \to 0$ and $Pm \ll 1$). Such a behaviour has been reported for several (helical and non-helical) forcing geometries (Brandenburg 2001; Ponty et al. 2004, 2005; Mininni et al. 2005; Mininni 2007; Ponty et al. 2007; Brandenburg 2009; Seshasayanan et al. 2017) and seems rather generic. For $\Omega_s \simeq 1\,\mathrm{d}^{-1}$, $R_* \simeq 2R_\odot$, and $Rm_c = 3000$, we obtain $\eta \lesssim 500\,\mathrm{m^2 s^{-1}}$ for $\epsilon_* = 10^{-8}$ and $\eta \lesssim 5 \times 10^5\,\mathrm{m^2 s^{-1}}$ for $\epsilon_* = 10^{-5}$. The latter values are acceptable values for stellar interiors, suggesting that stellar interiors may host dynamo capable flows.

We relate the dipolar field strength at the stellar surface B_0 to the amplitude of the flow (17) using the dimensionless parameter δ as

$$B_0 = \delta\,\epsilon_*\sqrt{\rho_*\mu_0}\,|\Omega_s - \Omega_{orb}|R_*, \tag{19}$$

In our simulations, the dipole amplitude at the surface B_0 is small compared to the typical magnetic field strength B_{rms} within the fluid (see Fig. 7), leading to $B_0^2 = f_1 E(\boldsymbol{B})$, or $B_0 = \sqrt{f_1}B_{rms}$, with $f_1 \simeq 10^{-4}$. The ratio of the magnetic energy to the kinetic energy is found to be $E(\boldsymbol{B})/E(\boldsymbol{u}) = f_2 = 0.01$ (see Fig. 6) in our simulations. By contrast, Barker & Lithwick (2013b) obtained $f_2 \approx 0.1$–0.3 in their magnetohydrodynamic simulations of the tidal instability within a periodic box. Actually, this ratio largely depends on supercriticality with respect to the dynamo onset. Equipartition cannot be excluded here in stellar interiors, hence we consider the range $f_2 \in [10^{-2}, 1]$. This results into $\delta = \sqrt{f_1 f_2} \in [10^{-3}, 10^{-2}]$. Making use of formula (13), the scaling law (19) can be written using astronomical quantities as

$$B_0 = \frac{3}{2}\sqrt{\frac{3\mu_0}{4\pi}}\delta\frac{R_*^{5/2}}{M_*^{1/2}}\Omega_s\frac{m}{D^3}\left|1 - \frac{\Omega_{orb}}{\Omega_s}\right|, \tag{20}$$

with the typical density $\rho_* = M_*/(4/3\pi R_*^3)$.

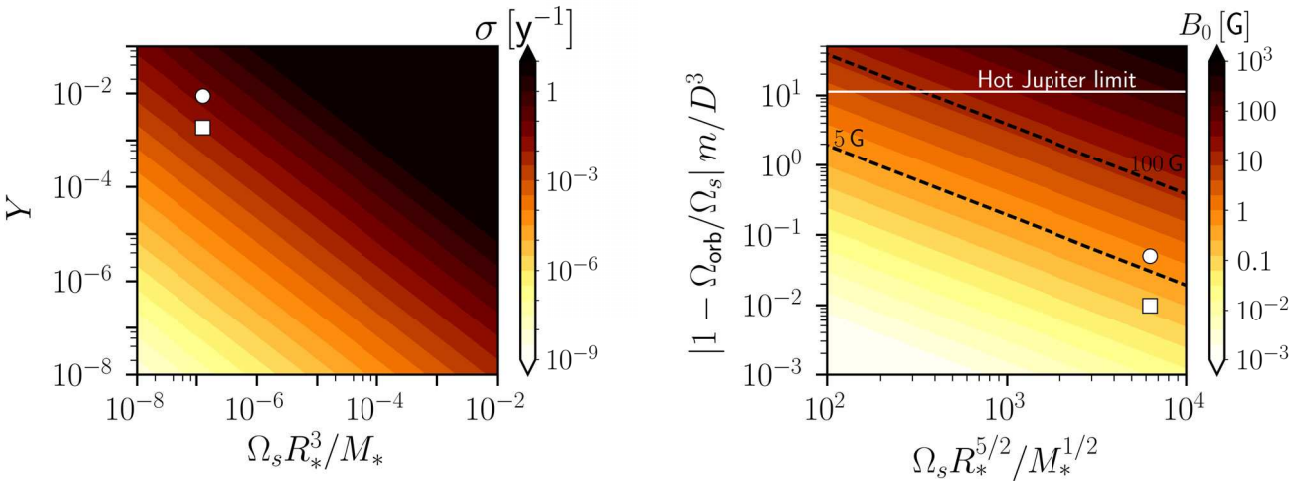

(a) Growth rate (b) Field strength

Figure 11. Predictions of the (a) growth rate (16) and (b) surface field strength (19) with $\delta = 10^{-3}$ for various stellar configurations. In (a), the vertical axis shows the quantity $Y = |1 - \Omega_{\rm orb}/\Omega_{\rm s}|(2\widetilde{\Omega}+3)^2/(16(1+\widetilde{\Omega})^2)m/D^3$. Horizontal solid white line in (b) shows the upper limit when the companion is a close and massive Hot Jupiter ($D = 0.01$ au, $m = 10\,M_{\rm J}$ with au the astronomical unit, and $M_{\rm J}$ the Jupiter mass. Tilted dashed lines show the orbital configurations associated with surface magnetic fields of 5 and 100 G. Circle (respectively square) point shows the location of Vega with an orbital companion characterized by $m = 1.24\,M_{\rm J}$, $D = 0.0165$ au, and $P_{\rm orb} = 0.53$ d (respectively $m = 0.34\,M_{\rm J}$, $D = 0.017$ au, and $P_{\rm orb} = 0.56$ d) as proposed by Boehm et al. (2015).

4.3 Comparison with convective dynamo scaling laws

In planetary or stellar convective dynamos, the viscous dissipation is expected to be negligible compared to the Ohmic one in the limit $Pm \ll 1$, as expected from turbulence studies (e.g. Brandenburg 2011). In this limit, Davidson (2013) argues that dynamo fields should be governed by

$$B_{\rm rms} \sim \sqrt{\rho_*\,\mu_0}\;(R_*\,\mathcal{P})^{1/3}, \tag{21}$$

where $\mathcal{P}$ is the power per unit mass injected into the dynamo capable flow (i.e. convection for convective dynamos, and tidal instability here). In this limit of vanishing viscous dissipation, it turns out that equation (21) is also consistent with the scaling laws obtained from usual convective dynamo simulations using the Boussinesq approximation (e.g. Schrinner et al. 2012; Yadav et al. 2013; Oruba & Dormy 2014). The power law given by equation (21) also holds for anelastic convection (Yadav & Christensen 2013). Thus, we can rely on equation (21) to compare convective dynamos scaling laws with our empirical scaling law (19).

To estimate $\mathcal{P}$, one can consider the tidal instability in a regime where viscous and ohmic dissipations are of the same order, such that any scaling law obtained for the viscous (or the ohmic) dissipation would also govern $\mathcal{P}$. This regime has been numerically studied by Barker & Lithwick (2013b) by imposing a weak magnetic field in a periodic box. They obtained that the dissipation rate per unit mass $\mathcal{D}_\nu$ is given by

$$\mathcal{D}_\nu = \chi(2R_*)^2|\Omega_{\rm s} - \Omega_{\rm orb}|^3\epsilon_*^3, \tag{22}$$

with $\chi \simeq 10^{-2}$. Hence, assuming $\mathcal{P} \sim \mathcal{D}_\nu$, equations (21) and (22) give the surface magnetic field $B_0 = f_1^{1/2}B_{\rm rms}$ as

$$B_0 \sim \delta\,\epsilon_*\sqrt{\rho_*\,\mu_0}\;|\Omega_{\rm s} - \Omega_{\rm orb}|R_*, \tag{23}$$

with $\delta = \sqrt{f_1 f_2}$ and $f_2 = (4\chi)^{2/3} \approx 0.1$. Thus, we recover equation (19) exactly. Moreover, Aubert et al. (2017) obtained $f_1 \approx 10^{-2}$ for a set of (convective) geodynamo simulations. Therefore, the scaling laws proposed for convective dynamo simulations are fully consistent with our scaling law (19), with a similar pre-factor $\delta \in [10^{-3}, 10^{-2}]$. This gives some confidence in the extrapolations to stars that follows.

We show in Fig. 11(a), the growth rate given by formula (16) and in Fig. 11(b) the surface field strength given by formula (19), for various orbital configurations. We have separated physical quantities of the orbital companion, (shown on the vertical axis) from stellar parameters (shown on the horizontal axis). Assuming that a Hot Jupiter is orbiting around the host star ($m \leq 10\,M_{\rm J}$ with $M_{\rm J}$ the Jupiter mass and $D \geq 0.01$ au), we expect magnetic field strengths ranging from sub-Gauss values to thousands of Gauss. Thus, tidal dynamos cannot be discarded in tidally deformed radiative stars with moderate stratification ($N_0/\Omega_{\rm s} \lesssim 2$–10).

4.4 Tidally driven dynamos in Vega-like stars?

Vega, with mass $M_* = 2.15\,{\rm M}_\odot$, radius $R_* = 2.5R_\odot$, and period $P_{\rm s} = 0.68$ d (Alina et al. 2012; Boehm et al. 2015) has a surface field strength of order $B_0 = 0.6 \pm 0.3$ G (Lignières et al. 2009; Petit et al. 2010). The fossil field theory predicts a field strength $B_0 = 20$ G (Braithwaite & Spruit 2017), 20–30 times too strong. To circumvent this issue, Braithwaite & Cantiello (2012) proposed that Vega contains a non-equilibrium fossil field undergoing dynamic evolution. Here, we provide an alternative scenario based on tidal forcing. Indeed, the recent discovery of starspots on Vega (Boehm et al. 2015) seem to support the existence of a close-in orbiting exoplanet. An exoplanet with a mass $m = 1.24\,M_{\rm J}$, at a distance $D = 0.0165$ au from the star, and with an orbital period $P_{\rm orb} = 0.53$ d or with a mass $m = 0.34\,M_{\rm J}$, at distance $D = 0.017$ au and with orbital period $P_{\rm orb} = 0.56$ d would support the astronomical observations (Boehm et al. 2015). With these parameters, the tidal instability would grow in a few thousand years for the two possible orbital configurations and would yield field strengths of $B_0 \simeq 8$ G for the first planetary configuration or $B_0 \simeq 1.5$ G for the second one, even though the system is close to synchronization. Although this

requires a moderate stratification, in the lower range of estimated values for Vega ($1 \leq N_0/\Omega_s \leq 25$ according to Rieutord 2006), the tidal dynamo model is consistent with the observed magnetic field of Vega. Therefore, Vega-like magnetism could well be due to tidally driven dynamos in tidally deformed bodies. Moreover, Petit et al. (2017) suggested that the time dependence of spots at the surface of Vega would support zonal flows, as we have observed in our simulations. This might be another hint supporting our tidal mechanism.

However, the existence of exoplanets around Vega remains controversial. Extended gaps in the debris discs around host stars are often attributed to tidal perturbations by Hot Jupiter planets. But within the current observational limits, no such massive planets have been detected undoubtedly around Vega (Su et al. 2013). Instead, Zheng et al. (2017) proposed a 'lone-planet' scenario to account for the observed structure with a single eccentric gas giant, with a mass $m = 3M_\mathrm{J}$ and located at the distance $D = 75$ au. This hypothetical exoplanet would be too far from Vega to induce strong tidal effects able to sustain a dynamo field.

4.5 Tidally driven dynamos in Ap/Bp stars?

Apart from weak Vega-like magnetism, we assess whether our mechanism is relevant to predict the large field strengths of other possibly tidally deformed magnetic stars, in particular Ap/Bp stars. Herbig Ae/Be stars, which are the precursors of magnetic Ap/Bp stars in the PMS phase, host magnetic fields with similar configurations than their MS counterparts (Alecian et al. 2012; Hubrig et al. 2014). Hence, it is believed that MS fields of Ap/Bp stars are already present at the PMS phase. About 70 per cent of the Herbig Ae/Be stars appear in binary/multiple systems (Baines et al. 2006), making them a priori good candidates for tidal dynamos. For instance, HD 200775 is known to be a non-synchronized binary system. The primary has a dipolar field strength of 1000 ± 150 G (Alecian et al. 2008). Yet, the tidal mechanism is unlikely to explain the observed magnetic field, because its intensity predicted using the characteristics of the binary system would be too weak from equation (20). Indeed, the distance D between the star and its companion is too large to induce strong tidal effects (orbital period of the companion is $P_\mathrm{orb} = 1412$ d and $D = 6.7$ au).

4.6 Tidal mixing

The relevance of the fossil field model is well established in chemically peculiar A/B stars (e.g. Braithwaite & Spruit 2017), in which an *in situ* magnetic generation by tides is not compatible with our findings. However, it is worth noting that it does not preclude the existence of the tidal instability within these bodies, in which it could play a dynamical role (without dynamo action). Indeed, Kama et al. (2015) suggest that giant planets of mass $m \simeq 0.1$–$10\,M_\mathrm{J}$ are hiding in at least 30 per cent of Herbig Ae/Be discs, possibly inducing strong tidal effects once on the MS (at least for the closest and most massive companions). Be stars are rapidly rotating MS B stars, such as HR 7355 (Oksala et al. 2010; Rivinius et al. 2012) and HR 5907 (Grunhut et al. 2011). Most massive stars ($M_* \geq 8\,\mathrm{M}_\odot$) either are binaries (about 75 per cent) or were so at some point in their evolution (Sana et al. 2012). Binarity is also a common feature in Be stars (Rivinius et al. 2013). Coupled with their rapid rotation periods, typically 0.5 d for HR 7355 (Oksala et al. 2010; Rivinius et al. 2012), the tidal instability could be significant in these binary systems (if they are not yet synchronized and if their stratification is not too strong).

5 CONCLUSION

5.1 Summary

We have numerically investigated the non-linear outcome of the tidal instability and assessed its dynamo capability in stellar radiative zones. We have adopted a simplified global model of the equilibrium tide in spherical containers. Its simplicity permits high-resolution numerical simulations using an efficient spectral code (Schaeffer 2013; Schaeffer et al. 2017).

We confirm that the basic equilibrium tide is prone to the tidal instability as reported by Cébron et al. (2010b). Furthermore, we have shown that this tidal instability is immune to a stable stratification as long as $N_0/\Omega_\mathrm{s} \lesssim 1$. In non-synchronized bodies, the instability grows on the typical time-scale $\epsilon_*^{-1}/|\Omega_\mathrm{s} - \Omega_\mathrm{orb}|$, yielding typically My for a star with a one-day spin period. The tidal instability induces non-linear motions, whose typical amplitude scales as $\epsilon_*|\Omega_\mathrm{s} - \Omega_\mathrm{orb}|R_*$ (Barker & Lithwick 2013b; Barker 2016), regardless of the stratification strength. These motions can induce radial mixing leading to self-consistent dynamos.

Time-averaged magnetic fields in our dynamos are mostly dipolar, an essential feature for their possible observations by astronomers. The dipolar field intensity at the surface is a small fraction δ of the magnetic intensity in the bulk. With our proof-of-concept simulations, we show that a tidal dynamo is a possible alternative mechanism to explain stellar magnetism of hot intermediate-mass and massive stars hosting close-in orbital companions.

Although motion amplitude being almost independent of the stratification, dynamo action was not found when the stratification is too large. Provided motion amplitude is large enough so that induction overcomes Ohmic dissipation ($Rm \gtrsim 3000$) and assuming the transitions between regimes occur at values of N_0/Ω_s independent of the diffusivities, tidally driven dynamos are likely when $N_0/\Omega_\mathrm{s} \leq 10$.

By extrapolating our results, we predict (i) a field strength up to several Gauss for presumably realistic orbital configurations (depending on the properties of the orbital companion, such as mass, distance to the host star), (ii) essentially all tidally deformed non-synchronized stars should have fields of strength at least comparable to Vega-like fields. Consequently, tidal dynamos in tidally deformed Vega-like stars could explain their magnetism, provided that they host a large and close enough companion and that their stratification is not too strong ($N_0/\Omega_\mathrm{s} \lesssim 2$–$10$ according to our simulations). Note also that all proposed mechanisms (e.g. failed fossil fields or innermost convective dynamos) are not mutually exclusive and may be combined to explain the observed fields.

5.2 Perspectives

Our proof-of-concept tidally driven dynamos call for many further studies, both to expand the surveyed parameter space and to refine the model. A considerable amount of work remains to be done to improve direct numerical simulations of tidal flows in stellar interiors, but we already hint at possible astrophysical consequences.

5.2.1 Parameter space exploration

We have not strived to adjust the dimensionless parameters to astrophysical realistic ones in the simulations. They are out of reach with the numerical resources currently available. The Reynolds number in well-mixed stars is expected to be huge and only the large-scale

components of the flow can be simulated. Consequently, the relatively high viscosity regime considered in our simulations may have filtered out tidal instabilities of smaller scales than those already obtained. We however expect that our proof-of-concept simulations capture the dominant global scales of tidally driven non-linear motions. We presume them not to be strongly dependent on resolving much smaller scales, but this is difficult to test numerically. Further simulations in the low diffusive regime, i.e. $Ek \to 0$, $Pr \ll 1$ and $Pm \ll 1$ are of interest, to study the robustness of tidally driven mixing and dynamo action. In particular, the dynamo capability in the region $1 < N_0/\Omega_s < 10$ must be studied with lower diffusivities. Indeed, the higher critical deformation for the onset of instability (see Appendix) is intriguing and prevents our current simulations to reliably assess the dynamo action in this range. It would be also worth to infer reliable scaling laws as diffusivities are lowered, especially the behaviour of δ with ϵ_* and Ek.

Stellar interiors have presumably small Prandtl numbers $10^{-8} \leq Pr \ll 1$ (e.g. Rieutord 2006). However, we have shown that some mixing is driven by the tidal instability. Mixed envelopes are often modelled by the assumption of equal turbulent diffusivities, yielding $Pr \lesssim 1$ (Zahn 1992). The sensitivity of the growth rate with Pr is briefly outlined in Appendix at $Ek = 10^{-4}$. The dependence on Pr should be better assessed in the future.

5.2.2 *Model refinements*

Anelastic models of stably stratified stars should be considered to better take into account buoyancy effects (Zahn et al. 2007; Simitev & Busse 2017). Note that the baroclinic instability has been ruled out from our model. Baroclinic instability is believed to occur in stars (Spruit & Knobloch 1984; Kitchatinov 2013, 2014). Only our basic state is barotropic, while the motions driven by the tidal instability are baroclinic. A baroclinic basic state is known to enhance the tidal instability in the equatorial plane of the star (Kerswell 1993; Le Bars & Le Dizès 2006). Moreover, baroclinic basic states generate non-linear motions which are also dynamo capable, as numerically shown by Simitev & Busse (2017). Consequently, a baroclinic tidal basic state could be even more dynamo capable and deserves further studies.

The influence of a more realistic geometry is also of interest. Indeed, we have assessed the dynamo capability in the simplest possible geometry of a full container. When a solid inner core is present, the tidal instability is also triggered in ellipsoidal shells (Cébron et al. 2012b). It is known that the global pattern of inertial modes is different in shells (Rieutord & Valdettaro 1997; Dintrans et al. 1999; Rieutord & Valdettaro 2010; Favier et al. 2014), which may affect the non-linear outcome of the tidal instability and ultimately its dynamo capability. However, first numerical (Cébron et al. 2010a,b) and experimental studies (Seyed-Mahmoud et al. 2004; Lemasquerier et al. 2017) in shells seem in agreement with results obtained in full containers.

5.2.3 *Possible astrophysical implications*

Statistically, it is believed that many magnetic stars host yet to be observed companions. If the tidal instability is responsible for stellar magnetic fields, then our mechanism provides constraints on the companion (e.g. mass and distance). Further astronomical observations should be carried out to clarify this point, by seeking signatures of orbital planetary companions (star–planets interactions) around magnetic stars or magnetic binaries (star–star interactions). Addressing the relevance of star–star interactions for magnetism of hot stars is one of the objectives of the BinaMIcS collaboration (Mathis et al. 2013; Alecian et al. 2015).

Then, interactions of the tidal instability with imposed fossil fields need also to be addressed. Even in the low Rm limit, in which dynamo action does not occur (if $Rm \leq Rm_c$), the tidal instability could develop against the stabilizing effect of the magnetic field in some stars and enhance the Ohmic dissipation of the fossil field due to the tidal mixing. Indeed, star–star interactions may explain that the magnetic incidence is much lower in binaries (less than 1.5 per cent) than in isolated stars (around 7 per cent), as for instance studied by the BinaMIcS collaboration (Alecian et al. 2015, 2017). Additionally, the time variability induced by the tidal instability may provide an alternative explanation for the observed temporal variability of strong fossil fields in Herbig Ae/Be stars, for instance in HD 190073 (Alecian et al. 2013).

Thus, there is an increasing need for stellar evolution models taking into account mixing in stellar radiative zones, which are often assumed to be motionless (Kippenhahn et al. 1990). This assumption is not justified because it does not account for various observational data (e.g. Pinsonneault 1997). Mixing has a strong impact on stellar evolution, for instance injecting hydrogen-rich material in the nuclear core or being responsible for the overabundance of some chemical elements at the surface of massive stars (e.g. Maeder & Meynet 2000). Various mechanisms have been proposed to account for the observed mixing, such as rotational mixing (Zahn 1992, 2008). Inertia-gravity waves could also partially account for the observed mixing (Press 1981; Garcia Lopez & Spruit 1991; Rogers et al. 2013). Inertia-gravity waves propagate in magnetic stars (e.g. Neiner et al. 2012) and can be excited by tidal forcing through direct resonances (e.g. Dintrans et al. 1999; Mirouh et al. 2016) or parametric resonances (as studied here). Mixing induced by the tidal instability has been so far overlooked in the models. However, we have shown that the tidal instability could lead to mixing in stably stratified fluids. Future studies should better quantify the tidal dissipation and mixing efficiency in radiative envelopes to improve future models of stellar evolution.

ACKNOWLEDGEMENTS

The XSHELLS and SHTNS codes are freely available at https://bitbucket.org/nschaeff/. The authors thank Stéphane Labrosse, Benjamin Favier, and Michael Le Bars for illuminating discussions about the physical interpretation of numerical results. JV and DC would like to thank Asif ud-Doula (Penn State Worhthington Scranton, Dunmore) for fruitful discussions and very helpful comments. DC and NS also thank François Lignières and Laurène Jouve for fruitful discussions at the meeting of the ANR IMAGINE (http://userpages.irap.omp.eu/ flignieres/index.html). This study was motivated by the BinaMIcS collaboration (Mathis et al. 2013; Alecian et al. 2015, 2017) and discussions with Stéphane Mathis and Evelyne Alecian. JV acknowledges the French Ministère de l'Enseignement Supérieur et de la Recherche for his PhD grant. The visit of JV at University of Leeds was supported by Labex OSUG@2020 (ANR10 LABX56) and by the doctoral school Terre Univers Environnement of Université Grenoble Alpes. We acknowledge GENCI for awarding us access to resource Occigen (CINES) under grants x2016047382 and x2017047382. Parts of the computations were also performed on the Froggy platform of CIMENT (https://ciment.ujf-grenoble.fr), supported by the Rhône-Alpes region (CPER07_13 CIRA), OSUG@2020 LabEx (ANR10

LABX56), and Equip@Meso (ANR10 EQPX-29-01). This work was partially funded by the French Agence Nationale de la Recherche under grant ANR-14-CE33-0012 (MagLune) and by the 2017 TelluS program from CNRS-INSU (PNP) AO2017-1040353. ISTerre is part of Labex OSUG@2020 (ANR10 LABX56). Most figures were produced using MATPLOTLIB (http://matplotlib.org/) or PARAVIEW (https://www.paraview.org/).

REFERENCES

Akgün T., Reisenegger A., Mastrano A., Marchant P., 2013, MNRAS, 433, 2445
Alecian E. et al., 2008, MNRAS, 385, 391
Alecian E. et al., 2012, MNRAS, 429, 1001
Alecian E., Neiner C., Mathis S., Catala C., Kochukhov O., Landstreet J., 2013, A&A, 549, L8
Alecian E. et al., 2015, in Meynet G., Georgy C., Groh J., Stee P., eds, Proc. IAU Symp. 307, New Windows on Massive Stars. Kluwer, Dordrecht, p. 330
Alecian E., Villebrun F., Grunhut J., Hussain G., Neiner C., Wade G. A., 2017, preprint (arXiv:1705.10650)
Alina D., Petit P., Lignières F., Wade G., Fares R., Aurière M., Böhm T., Carfantan H., 2012, in Hoffman J. L., Bjorkman J., Whitney B., eds, AIP Conf. Ser. Vol. 1429. Am. Inst. Phys., New York, p. 82
Arlt R., Rüdiger G., 2011a, Astron. Nachr., 332, 70
Arlt R., Rüdiger G., 2011b, MNRAS, 412, 107
Arlt R., Hollerbach R., Rüdiger G., 2003, A&A, 401, 1087
Aubert J., Gastine T., Fournier A., 2017, J. Fluid Mech., 813, 558
Augustson K., Mathis S., Brun A. S., 2017, Proc., 19th Workshop on Cool Stars, Stellar Systems, and the Sun, Simple scaling relationships for stellar dynamos. Cambridge, p. 152
Aurière M. et al., 2007, A&A, 475, 1053
Babcock H. W., 1947, ApJ, 105, 105
Baines D., Oudmaijer R. D., Porter J. M., Pozzo M., 2006, MNRAS, 367, 737
Balbus S. A., Hawley J. F., 1991, ApJ, 376, 214
Barker A. J., 2016, MNRAS, 459, 939
Barker A. J., Lithwick Y., 2013a, MNRAS, 435, 3614
Barker A. J., Lithwick Y., 2013b, MNRAS, 437, 305
Barker A. J., Braviner H. J., Ogilvie G. I., 2016, MNRAS, 459, 924
Behrend R., Maeder A., 2001, A&A, 373, 190
Blazère A., Neiner C., Petit P., 2016a, MNRAS, 459, L81
Blazère A. et al., 2016b, A&A, 586, A97
Boehm T. et al., 2015, A&A, 577, A64
Borra E. F., Landstreet J. D., Mestel L., 1982, ARA&A, 20, 191
Braithwaite J., 2006, A&A, 449, 451
Braithwaite J., Cantiello M., 2012, MNRAS, 428, 2789
Braithwaite J., Spruit H. C., 2004, Nature, 431, 819
Braithwaite J., Spruit H. C., 2017, R. Soc. Open Sci., 4, 160271
Brandenburg A., 2001, ApJ, 550, 824
Brandenburg A., 2009, ApJ, 697, 1206
Brandenburg A., 2011, ApJ, 741, 92
Brun A. S., Miesch M. S., Toomre J., 2004, ApJ, 614, 1073
Bullard E., Gellman H., 1954, Phil. Trans. R. Soc. A, Math. Phys. Sci, 247, 213
Busse F. H., 1970, J. Fluid Mech., 44, 441
Buysschaert B., Neiner C., Briquet M., Aerts C., 2017, A&A, 605, A104
Cantiello M., Braithwaite J., 2011, A&A, 534, A140
Cébron D., Hollerbach R., 2014, ApJ, 789, L25
Cébron D., Le Bars M., Leontini J., Maubert P., Le Gal P., 2010a, Phys. Earth Planet. Inter., 182, 119
Cébron D., Maubert P., Le Bars M., 2010b, Geophys. J. Int., 182, 1311
Cébron D., Le Bars M., Maubert P., Le Gal P., 2012a, Geophys. Astrophys. Fluid Dyn., 106, 524
Cébron D., Le Bars M., Moutou C., Le Gal P., 2012b, A&A, 539, A78
Cébron D., Le Bars M., Le Gal P., Moutou C., Leconte J., Sauret A., 2013, Icarus, 226, 1642
Charbonneau P., 2014, ARA&A, 52, 251
Charbonneau P., MacGregor K. B., 2001, ApJ, 559, 1094
Christensen U. R., Holzwarth V., Reiners A., 2009, Nature, 457, 167
Davidson P., 2013, Geophys. J. Int., 195, 67
Dintrans B., Rieutord M., Valdettaro L., 1999, J. Fluid Mech., 398, 271
Donati J.-F., Landstreet J. D., 2009, ARA&A, 47, 333
Fares R. et al., 2009, MNRAS, 398, 1383
Fares R. et al., 2012, MNRAS, 423, 1006
Fares R. et al., 2017, MNRAS, 471, 1246
Favier B., Barker A. J., Baruteau C., Ogilvie G. I., 2014, MNRAS, 439, 845
Favier B., Grannan A. M., Le Bars M., Aurnou J. M., 2015, Phys. Fluids, 27, 066601
Featherstone N. A., Browning M. K., Brun A. S., Toomre J., 2009, ApJ, 705, 1000
Ferriz-Mas A., Schmitt D., Schüssler M., 1994, A&A, 289, 949
Friedlander S., Siegmann W. L., 1982, Geophys. Astrophys. Fluid Dyn., 19, 267
Garcia Lopez R. J., Spruit H. C., 1991, ApJ, 377, 268
Gellert M., Rüdiger G., Hollerbach R., 2011, MNRAS, 414, 2696
Glatzmaier G. A., Roberts P. H., 1995, Nature, 377, 203
Goepfert O., Tilgner A., 2016, New J. Phys., 18, 103019
Goodman J., 1993, ApJ, 406, 596
Grannan A. M., Favier B., Le Bars M., Aurnou J. M., 2016, Geophys. J. Int., 208, 1690
Grunhut J. H. et al., 2011, MNRAS, 419, 1610
Guervilly C., Cardin P., 2010, Geophys. Astrophys. Fluid Dyn., 104, 221
Guervilly C., Hughes D. W., Jones C. A., 2014, J. Fluid Mech., 758, 407
Guervilly C., Hughes D. W., Jones C. A., 2015, Phys. Rev. E, 91, 041001
Hale G. E., 1908, ApJ, 28, 315
Herreman W., Cébron D., Le Dizès S., Le Gal P., 2010, J. Fluid Mech., 661, 130
Hubrig S., Briquet M., Schöller M., De Cat P., Mathys G., Aerts C., 2006, MNRAS, 369, L61
Hubrig S., Ilyin I., Schöller M., Cowley C. R., Castelli F., Stelzer B., Gonzalez J.-F., Wolff B., 2014, EPJ Web Conf., 64, 08006
Jouve L., Brun A. S., 2007, A&A, 474, 239
Jouve L., Brown B. P., Brun A. S., 2010, A&A, 509, A32
Jouve L., Gastine T., Lignières F., 2015, A&A, 575, A106
Kaiser R., Busse F., 2017, Geophys. Astrophys. Fluid Dyn., 111, 355
Kama M., Folsom C. P., Pinilla P., 2015, A&A, 582, L10
Kerswell R. R., 1993, Geophys. Astrophys. Fluid Dyn., 71, 105
Kerswell R. R., 2002, Annu. Rev. Fluid Mech., 34, 83
Kippenhahn R., Weigert A., Weiss A., 1990, Stellar Structure and Evolution. Springer, Berlin
Kitchatinov L. L., 2013, Astron. Lett., 39, 561
Kitchatinov L. L., 2014, ApJ, 784, 81
Kochukhov O., Sudnik N., 2013, A&A, 554, A93
Lacaze L., Herreman W., Le Bars M., Le Dizès S., Le Gal P., 2006, Geophys. Astrophys. Fluid Dyn., 100, 299
Larmor J., 1919, Rep. Brit. Assoc. Adv. Sci, 159, 412
Le Bars M., Le Dizès S., 2006, J. Fluid Mech., 563, 189
Le Bars M., Lacaze L., Le Dizès S., Le Gal P., Rieutord M., 2010, Phys. Earth Planet. Inter., 178, 48
Le Reun T., Favier B., Barker A. J., Le Bars M., 2017, Phys. Rev. Lett., 119, 034502
Lemasquerier D., Grannan A. M., Vidal J., Cébron D., Favier B., Le Bars M., Aurnou J. M., 2017, J. Geophys. Res.: Planets, 122, 1926
Lewis H. R., Bellan P. M., 1990, J. Math. Phys., 31, 2592
Lignières F., Petit P., Böhm T., Auriere M., 2009, A&A, 500, L41
Lignières F., Petit P., Aurière M., Wade G. A., Böhm T., 2013, in Petit P., Jardine M., Spruit H. C., eds, Proc. IAU Symp. 9, Magnetic Fields throughout Stellar Evolution. Kluwer, Dordrecht, p. 338
Lin Y., Ogilvie G. I., 2017, MNRAS, 468, 1387
Livermore P. W., Bailey L. M., Hollerbach R., 2016, Sci. Rep., 6, 22812
MacDonald J., Mullan D. J., 2004, MNRAS, 348, 702
MacGregor K. B., Cassinelli J. P., 2003, ApJ, 586, 480
Maeder A., Meynet G., 2000, ARA&A, 38, 143
Marcotte F., Gissinger C., 2016, Phys. Rev. Fluid, 1, 063602

Markey P., Tayler R. J., 1973, MNRAS, 163, 77
Marti P. et al., 2014, Geophys. J. Int., 197, 119
Mathis S., Neiner C., Alecian E., Wade G., 2013, in Petit P., Jardine M., Spruit H. C., eds, Proc. IAU Symp. 9, Magnetic Fields throughout Stellar Evolution. Kluwer, Dordrecht, p. 311
Mathys G., 2017, A&A, 601, A14
Matsui H. et al., 2016, Geochem. Geophys. Geosyst., 17, 1586
Mininni P. D., 2007, Phys. Rev. E, 76, 026316
Mininni P. D., Ponty Y., Montgomery D. C., Pinton J.-F., Politano H., Pouquet A., 2005, ApJ, 626, 853
Mirouh G. M., Baruteau C., Rieutord M., Ballot J., 2016, J. Fluid Mech., 800, 213
Miyazaki T., 1993, Phys. Fluids A: Fluid Dyn., 5, 2702
Mizerski K. A., Lyra W., 2012, J. Fluid Mech., 698, 358
Mizerski K. A., Bajer K., Moffatt H. K., 2012, J. Fluid Mech., 707, 111
Moss D., 1989, MNRAS, 236, 629
Neiner C. et al., 2012, A&A, 546, A47
Neiner C., Mathis S., Alecian E., Emeriau C., Grunhut J., 2014, in Nagendra K. N., Bagnulo S., Centeno R., Jesús Martínez González M., eds, Proc. IAU Symp. 10, Polarimetry: From the {Sun} to Stars and Stellar Environments. Cambridge Univ. Press, p. 61
Ogilvie G. I., 2005, J. Fluid Mech., 543, 19
Ogilvie G. I., 2013, MNRAS, 429, 613
Oksala M. E., Wade G. A., Marcolino W. L. F., Grunhut J., Bohlender D., Manset N., Townsend R. H. D., 2010, MNRAS, 405, L51
Oruba L., Dormy E., 2014, Geophys. J. Int., 198, 828
Palla F., Stahler S. W., 1992, ApJ, 392, 667
Parker E. N., 1955, ApJ, 122, 293
Parker E. N., 1975, ApJ, 198, 205
Parker E. N., 1979, Cosmical Magnetic Fields: Their Origin and Their Activity. Clarendon Press; Oxford University Press, Oxford
Petit P. et al., 2010, A&A, 523, A41
Petit P. et al., 2011, A&A, 532, L13
Petit P., Hébrard E. M., Böhm T., Folsom C. P., Lignières F., 2017, MNRAS, 472, L30
Pinsonneault M., 1997, ARA&A, 35, 557
Pitts E., Tayler R. J., 1985, MNRAS, 216, 139
Ponty Y., Politano H., Pinton J.-F., 2004, Phys. Rev. Lett., 92, 144503
Ponty Y., Mininni P. D., Montgomery D. C., Pinton J.-F., Politano H., Pouquet A., 2005, Phys. Rev. Lett., 94, 164502
Ponty Y., Mininni P. D., Pinton J.-F., Politano H., Pouquet A., 2007, New J. Phys., 9, 296
Potter A. T., Chitre S. M., Tout C. A., 2012, MNRAS, 424, 2358
Power J., Wade G. A., Aurière M., Silvester J., Hanes D., 2008, Contrib. Astron. Obs. Skalnaté Pleso, 38, 443
Press W. H., 1981, ApJ, 245, 286
Remus F., Mathis S., Zahn J.-P., 2012, A&A, 544, A132
Rieutord M., 2001, ApJ, 550, 443
Rieutord M., 2004, in Maeder A., Eenens P., eds, Proc. IAU Symp. 215, Stellar Rotation. Astron. Soc. Pac., San Francisco, p. 394
Rieutord M., 2006, A&A, 451, 1025
Rieutord M., Valdettaro L., 1997, J. Fluid Mech., 341, 77
Rieutord M., Valdettaro L., 2010, J. Fluid Mech., 643, 363
Rivinius T., Townsend R. H. D., Kochukhov O., Štefl S., Baade D., Barrera L., Szeifert T., 2012, MNRAS, 429, 177
Rivinius T., Carciofi A. C., Martayan C., 2013, A&AR, 21, 69
Roberts P. H., 1968, Phil. Trans. R. Soc. A: Math. Phys. Eng. Sci., 263, 93
Rogers T. M., Lin D., McElwaine J. N., Lau H. H. B., 2013, ApJ, 772, 21
Sana H. et al., 2012, Science, 337, 444
Schaeffer N., 2013, Geochem. Geophys. Geosyst., 14, 751
Schaeffer N., Jault D., Nataf H.-C., Fournier A., 2017, Geophys. J. Int., 211, 1
Schrinner M., Petitdemange L., Dormy E., 2012, ApJ, 752, 121
Seilmayer M., Stefani F., Gundrum T., Weier T., Gerbeth G., Gellert M., Rüdiger G., 2012, Phys. Rev. Lett., 108, 244501
Seshasayanan K., Gallet B., Alexakis A., 2017, Phys. Rev. Lett., 119, 204503
Seyed-Mahmoud B., Aldridge K., Henderson G., 2004, Phys. Earth Planet. Inter., 142, 257
Simitev R. D., Busse F. H., 2017, Geophys. Astrophys. Fluid Dyn., 111, 369
Spiegel E. A., Veronis G., 1960, ApJ, 131, 442
Spruit H. C., 1999, A&A, 349, 189
Spruit H. C., 2002, A&A, 381, 923
Spruit H. C., Knobloch E., 1984, A&A, 132, 89
Stefani F., Giesecke A., Weber N., Weier T., 2016, Solar Phys., 291, 2197
Stello D., Cantiello M., Fuller J., Huber D., García R. A., Bedding T. R., Bildsten L., Aguirre V. S., 2016, Nature, 529, 364
Strugarek A., Beaudoin P., Charbonneau P., Brun A. S., do Nascimento J.-D., 2017, Science, 357, 185
Su K. Y. et al., 2013, ApJ, 763, 118
Szklarski J., Arlt R., 2013, A&A, 550, A94
Tayler R., 1973, MNRAS, 161, 365
Tilgner A., 2005, Phys. Fluids, 17, 034104
Vantieghem S., Cébron D., Noir J., 2015, J. Fluid Mech., 771, 193
Vidal J., Cébron D., 2017, J. Fluid Mech., 833, 469
Weber N., Galindo V., Stefani F., Weier T., 2015, New J. Phys., 17, 113013
Wu C.-C., Roberts P. H., 2009, Geophys. Astrophys. Fluid Dyn., 103, 467
Yadav R. K., Gastine T., Christensen U. R., 2013, Icarus, 225, 185
Yadav R. K., Gastine T., Christensen U. R., Duarte L. D. V., 2013, ApJ, 774, 6
Zahn J.-P., 1966, Ann. Astrophys., 29, 313
Zahn J.-P., 1992, A&A, 265, 115
Zahn J.-P., 2008, in Deng L., Chan K. L., eds, Proc. IAU Symp. 4, The Art of Modeling Stars in the 21st Century. Kluwer, Dordrecht, p. 47
Zahn J.-P., Brun A. S., Mathis S., 2007, A&A, 474, 145
Zhang K., Chan K. H., Zou J., Liao X., Schubert G., 2003, ApJ, 596, 663
Zheng X., Lin D. N. C., Kouwenhoven M. B. N., Mao S., Zhang X., 2017, ApJ, 849, 98

APPENDIX: WEAKENING OF THE TIDAL INSTABILITY WHEN $1 \lesssim N_0/\Omega_s \leq 2$

The energy collapse of non-linear flows in Fig. 2(b), responsible for the absence of mixing in Fig. 9(b) when $1 \leq N_0/\Omega_s \leq 2$, is due to diffusive effects at the moderately small value $Ek = 10^{-4}$ and $Pr = 1$. We performed simulations at $Ek = 10^{-4}$ and $Pr = 0.1$, i.e. for a thermal diffusion 10 times larger than viscous diffusion. In Fig. A1, we show the normalized growth rate σ/ϵ_c for varying N_0/Ω_s. When $N_0/\Omega_s \lesssim 1$ the growth rates for both $Pr = 1$ and 0.1 are weakly affected and almost insensitive to N_0/Ω_s. However for stronger stratifications, the growth rates are strongly reduced. When $1.5 \leq N_0/\Omega_s \leq 2$, the tidal instability is even lost in simulations at $\epsilon = 0.2$. Thus, the critical ellipticity ϵ_c above which the tidal instability is triggered evolves with N_0/Ω_s at our moderate Ekman number. To quantify this effect, we show in Fig. A2 how ϵ_c evolves as a function of N_0/Ω_s. In the range of interest $1 \leq N_0/\Omega_s \leq 2$, ϵ_c quickly increases with N_0^2/Ω_s^2. Hence, non-linear curves in

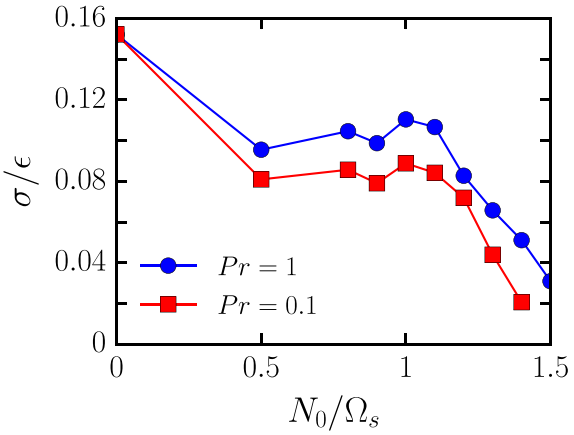

Figure A1. Normalized growth rate of the tidal instability σ/ϵ for varying N_0/Ω_s. Simulations at $Ek = 10^{-4}$, $\epsilon = 0.2$, $Pr = 1$ (circles), and $Pr = 0.1$ (squares).

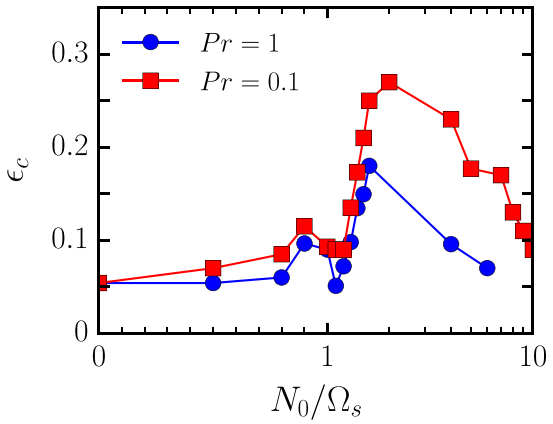

Figure A2. Threshold ϵ_c of the tidal instability for varying N_0/Ω_s. Simulations at $Ek = 10^{-4}$, $Pr = 1$ (circles), and $Pr = 0.1$ (squares). To determine ϵ_c, we have performed simulations for several ellipticity ϵ. Horizontal axis is linear between 0 and 1, then it is logarithmic.

Figs 2(b) and 9(b) have not been obtained for a constant supercriticality ϵ/ϵ_c. This phenomenon explains why the amplitude of non-linear flows quickly drops for $1 \leq N_0/\Omega_s \leq 2$, because simulations at $N_0/\Omega_s \leq 1$ are about four times critical, while the ones at $1 \leq N_0/\Omega_s \leq 2$ are only barely supercritical. Finally, for stronger stratification ($N_0/\Omega_s \gg 2$), the threshold ϵ_c decreases back to values close to the ones without stratification. This is the reason why we observe the onset of the tidal instability for these stratifications in Fig. 2. The more N_0/Ω_s increases, the more radial motions are inhibited and become of short wavelength in the linear growth of the instability and toroidal motions are favoured. The latter motions are the least diffusively damped flows with stress-free boundary conditions (e.g. Rieutord 2001). Hence, the combined effects of diffusion and stronger stratification favour toroidal motions and decrease the threshold of the tidal instability.

This paper has been typeset from a TEX/LATEX file prepared by the author.